Biophysical Journal Volume 107 December 2014 2546–2558

Article

3D Collagen Alignment Limits Protrusions to Enhance Breast Cancer Cell Persistence

Kristin M. Riching,[1,2] Benjamin L. Cox,[2,3] Max R. Salick,[4,5] Carolyn Pehlke,[2] Andrew S. Riching,[6] Susan M. Ponik,[6] Benjamin R. Bass,[8] Wendy C. Crone,[1,4,5] Yi Jiang,[9] Alissa M. Weaver,[10] Kevin W. Eliceiri,[1,2,7] and Patricia J. Keely[1,2,6,7,*]

[1]Biomedical Engineering Program, [2]Laboratory for Optical and Computational Instrumentation, [3]Department of Medical Physics, [4]Materials Science Program, [5]Department of Engineering Physics, [6]Department of Cell and Regenerative Biology, and [7]University of Wisconsin Paul P. Carbone Comprehensive Cancer Center, University of Wisconsin-Madison, Madison, Wisconsin; [8]Saris Cycling Group, Madison, Wisconsin; [9]Department of Mathematics and Statistics, Georgia State University, Atlanta, Georgia; and [10]Department of Cancer Biology, Vanderbilt University Medical Center, Nashville, Tennessee

ABSTRACT Patients with mammographically dense breast tissue have a greatly increased risk of developing breast cancer. Dense breast tissue contains more stromal collagen, which contributes to increased matrix stiffness and alters normal cellular responses. Stromal collagen within and surrounding mammary tumors is frequently aligned and reoriented perpendicular to the tumor boundary. We have shown that aligned collagen predicts poor outcome in breast cancer patients, and postulate this is because it facilitates invasion by providing tracks on which cells migrate out of the tumor. However, the mechanisms by which alignment may promote migration are not understood. Here, we investigated the contribution of matrix stiffness and alignment to cell migration speed and persistence. Mechanical measurements of the stiffness of collagen matrices with varying density and alignment were compared with the results of a 3D microchannel alignment assay to quantify cell migration. We further interpreted the experimental results using a computational model of cell migration. We find that collagen alignment confers an increase in stiffness, but does not increase the speed of migrating cells. Instead, alignment enhances the efficiency of migration by increasing directional persistence and restricting protrusions along aligned fibers, resulting in a greater distance traveled. These results suggest that matrix topography, rather than stiffness, is the dominant feature by which an aligned matrix can enhance invasion through 3D collagen matrices.

INTRODUCTION

Increased mammographic density is associated with a 4- to 6-fold increased risk of breast cancer (1–3), making mammographic density one of the greatest independent risk factors for breast cancer (1,3,4). This increase in density is correlated with a significantly increased deposition of extracellular matrix (ECM) proteins, most notably collagen I (5–7), which is in part responsible for the overall increase in stiffness in mammary tumors (8,9). Matrix stiffness has been shown to promote a malignant phenotype in tumor cells (8,10–12), enhance migration and invasion (13–16), and alter cell signaling, leading to increased proliferation (10,17–19). Although it is clear that matrix stiffness plays a profound role in tumor progression, we do not yet fully understand the mechanisms by which cells respond to changes in matrix stiffness.

In addition to the amount of collagen, the orientation of collagen fibers appears to play a critical role in tumor progression. Our laboratory previously characterized changes in the alignment and orientation of collagen fibers, and identified tumor-associated collagen signatures (TACS), which manifest in predictable ways during tumor progression. In particular, deposition of aligned collagen that is oriented perpendicular to the tumor boundary (termed TACS-3) creates highways on which tumor cells are observed to migrate in vivo (20), and correlates with increased invasion and metastasis in mouse models (21). More recently, we showed that TACS-3 alignment is an independent prognostic signature that correlates strongly with poor patient survival (22). These initial findings strongly indicate that matrix stiffness resulting from increased collagen deposition and matrix alignment contributes to mammary tumor progression.

Although the cellular players and mechanism for alignment generation in vivo remain elusive, in vitro studies have shown that epithelial cells and fibroblasts are capable of using Rho- and Rho kinase (ROCK)-mediated actin-myosin contractility to orient collagen fibers (23–26). Additionally, fibroblasts can deposit matrices containing aligned fibronectin or collagen in vitro (27,28). Recently, Yang et al. (28) showed that this ability of fibroblasts to produce aligned matrices is associated with expression of the cell-surface proteoglycan syndecan-1.

The high correlation of collagen alignment with breast tumor progression suggests that the mechanisms by which alignment facilitates cell migration need to be evaluated more closely. Studies of cells cultured in matrices with

Submitted May 8, 2014, and accepted for publication October 3, 2014.

*Correspondence: pjkeely@wisc.edu

Editor: David Odde.

0006-3495/14/12/2546/13 $2.00

http://dx.doi.org/10.1016/j.bpj.2014.10.035

aligned fibers have revealed that cells polarize and orient with respect to the alignment (29–31), and that alignment is associated with increased migration and directionality (23,28,32). The underlying mechanisms for these responses to alignment, however, remain unclear. One possibility is that alignment organizes cell adhesions along fibers, resulting in more efficient migration from coordinated traction forces. It has been demonstrated that parallel-oriented fibers may also afford cells less spatial impedance and thereby enhance migration (33). Additionally, it has been suggested that alignment incurs changes in matrix stiffness, and that enhanced migration along fibers may be due to durotactic guidance. However, the effects of increasing alignment on tensile modulus have been largely assumed, without being well documented and quantified. Here, we created novel (to our knowledge) aligned matrices to parse out the contributions of 3D matrix alignment and stiffness to the migration of breast cancer cells. We find that alignment facilitates persistence without affecting migration speed, and that contact guidance via aligned fibers, rather than durotaxis due to stiffness, is the likely mechanism by which migration is enhanced. Moreover, we present a model to describe trends in cell migration induced by matrix physical and mechanical properties. Validating the model's prediction, we found that an aligned matrix limits the number of stabilized protrusions and likely serves as mechanism that leads to more persistent migration.

RESULTS

The aim of this study was to characterize the effects of collagen fiber alignment and matrix stiffness on the 3D cell migration of invasive ductal breast carcinoma cells. To study the mechanical properties of aligned collagen and how cells respond to changing matrix mechanics, we generated 3D collagen gels containing aligned fibers by using a device to impart mechanical strain. Similar to the method described by Vader et al. (34), we designed and used a 3D printer to create a strain device that uses a micrometer-driven arm and pin assembly to stretch one end of a collagen gel (Fig. 1 *A*). The pins contacted two pieces of polypropylene mesh embedded in the gel and had a width of 1 cm to produce a wide aligned region. The device was designed to fit the stage of a multiphoton microscope, and second harmonic generation (SHG) images of a 2 mg/ml gel were collected with increasing strain applied (Fig. 1 *B*). We used CurveAlign software (http://www.loci.wisc.edu) analysis, which employs a curvelet-based algorithm to measure fiber orientation and assigns a coefficient of alignment from zero (no alignment of one fiber relative to another) to one (all fibers in perfect alignment). The coefficient of alignment increased with strain and appeared to approach a maximum alignment at 30% strain (Fig. 1 *C*).

To determine whether aligned collagen had a greater elastic modulus than gels with randomly oriented fibers, we cast 2 mg/ml collagen gels in a stainless-steel, dog-bone-shaped mold that was machined to the dimensions specified in Roeder et al. (35). We then tested the tensile moduli of the gels using an Instron MicroTester 5548. (For an image of a representative collagen gel in the grips of the Instron, see Fig. S1 B in the Supporting Material.) Samples were either prestrained using the strain device shown in Fig. 1 or left unstrained. All samples were imaged via SHG to observe the fiber alignment and then subjected to tensile testing at a rate of 1 mm/min until failure occurred. Sample strain was computed by measuring

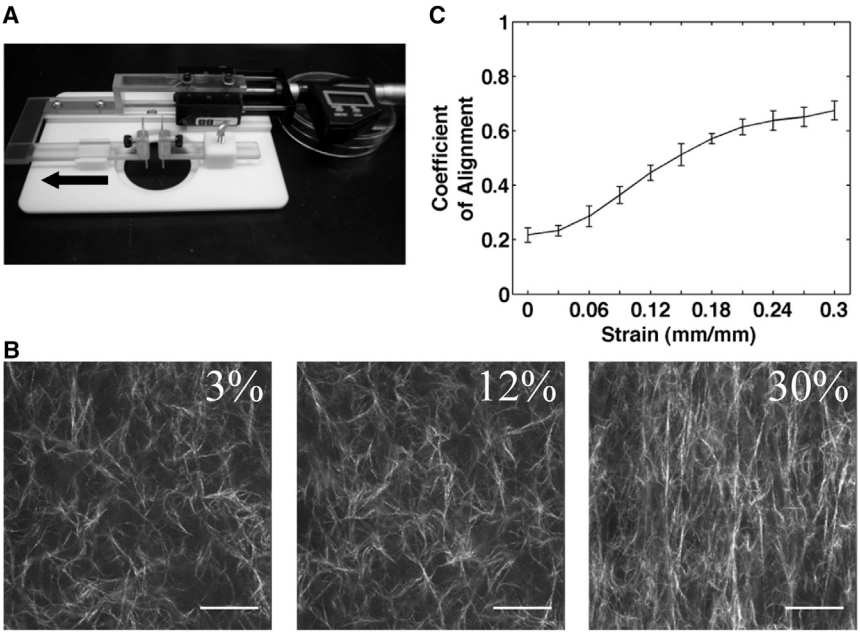

FIGURE 1 Collagen gels are aligned by mechanical strain. (*A*) A strain device designed and assembled for use with a multiphoton microscope is fitted with a micrometer to precisely control the amount of strain on a collagen gel placed in the center of the stage. Two pins contact the sample and the left pin/arm assembly is driven by a micrometer. The arrow indicates the direction of strain. (*B*) SHG images reveal collagen fiber alignment with increasing strain; scale bar, 50 μm. (*C*) CurveAlign software analysis of coefficient of alignment from SHG images ($n = 3$ gels).

the relative displacement of glass beads deposited on the surface of the gel. All prestrained samples demonstrated an increased coefficient of alignment due to an increase in the number of fibers oriented near 0° relative to the axis of the dogbone (71% of fibers for prestrained samples compared with 43% for unstrained samples; Fig. 2, A, *left* and *right*).

Stress-strain curves for unstrained samples displayed classic strain-stiffening behavior with the presence of a toe region, indicative of fiber recruitment, before the linear regime. In contrast, prestrained gels lacked a toe region, consistent with the prealignment of fibers, and the linear regime exhibited a steeper slope (Fig. 2 *B*). The slope of this linear regime represents the elastic modulus, and prestrained gels had greater elastic moduli than unstrained gels regardless of whether the gels were left unfixed (Fig. 2 *C*, *right*) or fixed using 4% paraformaldehyde (PFA) for 10 min immediately after prestraining (Fig. 2 *C*, *left*). Thus, prealigning the collagen matrix alters the elastic behavior and results in a significant increase in the stiffness of the matrix.

Cells are known to use durotaxis to migrate toward increased stiffness (13). Since we previously showed that cells preferentially migrate along, rather than across, aligned fibers (23), we tested whether the elastic modulus is greater along the axis of aligned fibers than across the axis of alignment. We prestrained large (2 mg/ml) collagen gels using a horizontal weight-based loading system that clamped two sides of a gel suspended in a PBS bath. One clamp remained stationary while the other was drawn with the use of weights to stretch the gel, and the gel was subsequently fixed with 4% PFA. A 3D-printed cutter was then used to cut dogbone-shaped specimens from the larger gel, with dimensions identical to those of the aforementioned dogbone mold. Specimens were cut such that the gauge region of the dogbone was either parallel or perpendicular to the direction of the applied strain (Fig. S1 A). Dogbones cut parallel to the direction of strain had aligned fibers oriented ~0° relative to the axis of alignment, whereas those cut perpendicular to the strain direction had fibers oriented ~90° (Fig. S1 D, *left*). The parallel and perpendicular cut gels had similar high coefficients of alignment (Fig. S1 D, *right*). However, the

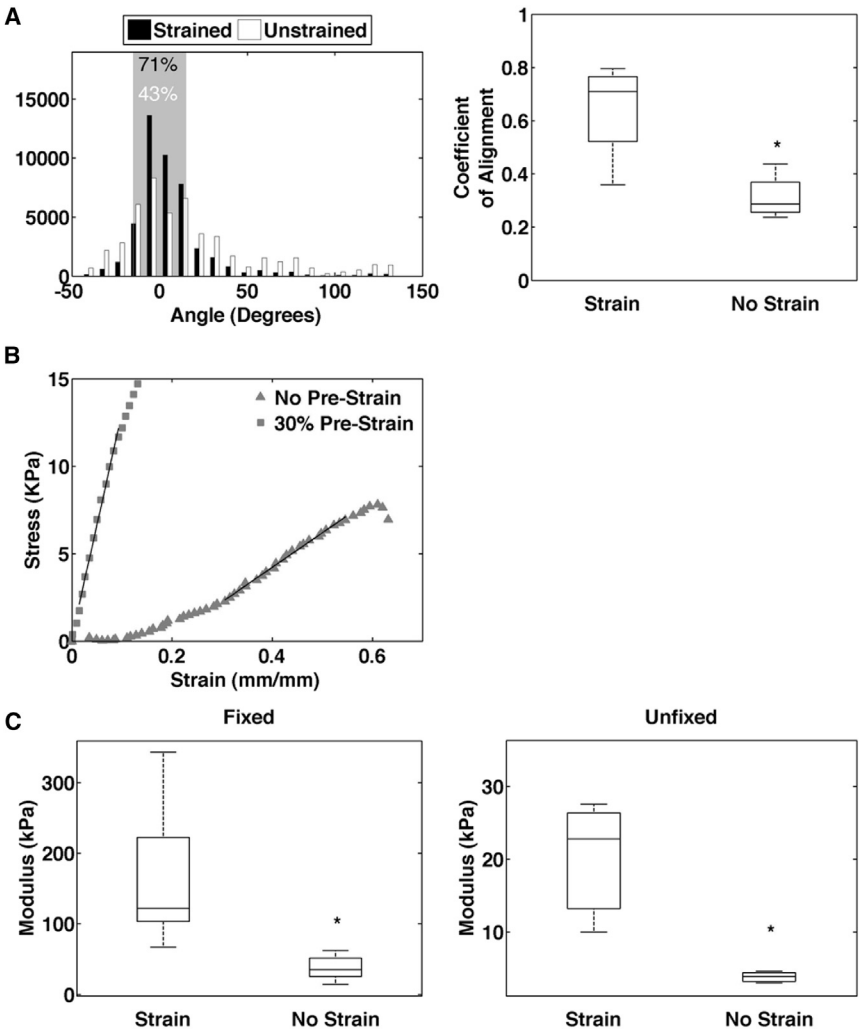

FIGURE 2 Aligned collagen gels are stiffer than unaligned gels. (*A*) Left: histograms of fiber angles generated from CurveAlign software of unstrained and 30% prestrained gels. Percentages represent the fraction of fiber angles ±15° from 0° relative to the axis of alignment (*shaded region*). (*A*) Right: coefficient of alignment of unstrained and 30% prestrained gels ($n = 4$ gels, $p < 0.05$). Note that even unstrained samples demonstrate fibers oriented at 0°, which is due to a stronger signal in this orientation because of laser polarization (36,37); however, all strained samples exceeded this background level. (*B*) Representative stress-strain curves of an unstrained gel and 30% prestrained gel fixed with PFA. (*C*) Tensile modulus of unstrained and 30% prestrained gels fixed with PFA ($n = 13$ gels, $p < 0.0001$) or unfixed ($n = 3$ gels, $p < 0.05$).

moduli were greatest in the parallel strained gels (Fig. S1 C), indicating that collagen is stiffest along the axis of alignment. Interestingly, the moduli for perpendicular strained and unstrained gels were similar, which served as a control for other effects of prestraining the collagen gel that were not related to orientation of the fibers.

To determine whether this increased stiffness along the axis of alignment leads cells to preferentially migrate along aligned collagen fibers, we conducted a set of experiments to assess MDA-MB-231 cell migration and matrix stiffness in aligned and random collagen gels with increasing collagen concentration. Initially, we determined the coefficient of alignment and elastic modulus for 1–4 mg/ml prestrained and unstrained collagen gels. These experiments showed that the coefficient of alignment was higher for all prestrained gels regardless of collagen concentration (Fig. 3 *A*). The elastic modulus increased with increasing collagen concentration for both prestrained and unstrained samples, with all prestrained specimens having a significantly greater modulus than their unstrained counterparts (Fig. 3 *B*). Note that the modulus of the 4 mg/ml unstrained specimens was not significantly different from that of the 1 mg/ml prestrained aligned gels, which serves below as a useful comparison for cell migration in matrices of different topography but identical stiffness.

After characterizing the stiffness of aligned and random collagen matrices across a range of concentrations, we sought to determine the effect of changing matrix stiffness and alignment on cell migration. As the cells were not readily seeded in a reproducible way into gels that were aligned by strain, we developed a flow-based 3D microchannel assay to produce either an aligned or a random collagen matrix based on other reports using microchannels (36,37). When neutralized collagen was flowed during polymerization through narrow channels (width = 1 mm), an aligned matrix was produced. Flowing polymerizing collagen through a wider channel (width = 3 mm) produced a random matrix (Fig. 3 *C*). MDA-MB-231 cells were seeded in the center ports of both narrow and wide channels and allowed to migrate for 3 days, after which time the gels were fixed and stained with bisbenzimide to assess the number of cells that migrated into the channel. SHG images were collected to assess fiber alignment in narrow (Fig. 3 *F*) and wide (Fig. 3 *G*) microchannels, and confocal images of stained nuclei (Fig. 3, *D* and *E*) were analyzed in FIJI. All narrow channels had a significantly higher coefficient of alignment compared with wide channels (Fig. 3 *H*). Moreover, all narrow channels had a greater number of cells that migrated farther away from the port (Fig. 3 *I*) compared with wide channels (Fig. 3 *J*).

To determine whether migration correlated with matrix alignment or stiffness, total nuclei counts outside of the port boundary were normalized to the channel width and plotted against either the coefficient of alignment or the tensile modulus. Cell counts displayed a positive correlation with the coefficient of alignment for all collagen concentrations (Fig. 3 *K*). In contrast, cell migration displayed a negative correlation with modulus across all concentrations for both narrow and wide channels (Fig. 3 *L*). These results indicate that alignment improves the efficiency of cell migration, whereas increasing the matrix stiffness by increasing the collagen concentration serves to impede migration, possibly because it offers cells too many sites for cell adhesion (38,39) or because increased collagen concentration increases cell confinement by decreasing porosity (40).

To further understand how aligned collagen enhances migration, we tested the effects of alignment on migration speed and persistence in 1 and 4 mg/ml collagen. We imaged MDA-MB-231 cells seeded into narrow and wide channels every 10 min over 6 h using a confocal microscope, and tracked migrating cells using the MTrackJ plugin for FIJI. For these experiments, we only considered collagen concentrations of 1 and 4 mg/ml because these concentrations represent the extremes measured for the tensile modulus, and because the stiffness of an aligned 1 mg/ml gel was comparable to that of a random 4 mg/ml gel (Fig. 3 *B*). Time-lapse movies of cell migration in 1 mg/ml narrow and wide channels were used to quantify cell migration (Movie S1). Windrose plots of all of the analyzed tracks show a greater percentage of cells migrating within 10° of the direction of alignment in 1 and 4 mg/ml narrow channels (Fig. 4 *A*).

We used the chemotactic index (CI), a measure of a cell's directional persistence that is traditionally used in reference to a chemotactic gradient, to measure the component of migration tracks in the direction of alignment, and found it to be highest in narrow channels (Fig. 4 *B*). Surprisingly, migration speed was unchanged between cells cultured in narrow and wide channels of the same collagen concentration (Fig. 4 *C*), suggesting that alignment does not affect cell speed. Moreover, cell speed was equivalently reduced at the higher collagen concentration despite the similar elastic moduli of 1 mg/ml aligned and 4 mg/ml random matrices (Fig. 3 *B*).

Histograms of individual cells' net displacements demonstrate that compared with cells in wide channels, cells that migrated in narrow channels more often ended up farther away from their starting points (Fig. 4, *D* and *E*). Although the channel widths differed between narrow and wide channels, the enhanced persistence seen in narrow channels is unlikely to result from the smaller geometry. If this were true, and the dimensions of the narrow channels restricted migration to a more confined region, we would expect to see preferential migration along the edges of the matrix near the channel wall where restriction is highest. In fact, we saw cells evenly distributed across the channel width, suggesting that changing channel geometry does not impact cell migration. Taken together, these results suggest that collagen alignment affects the directional persistence, but not the speed, of migrating cells.

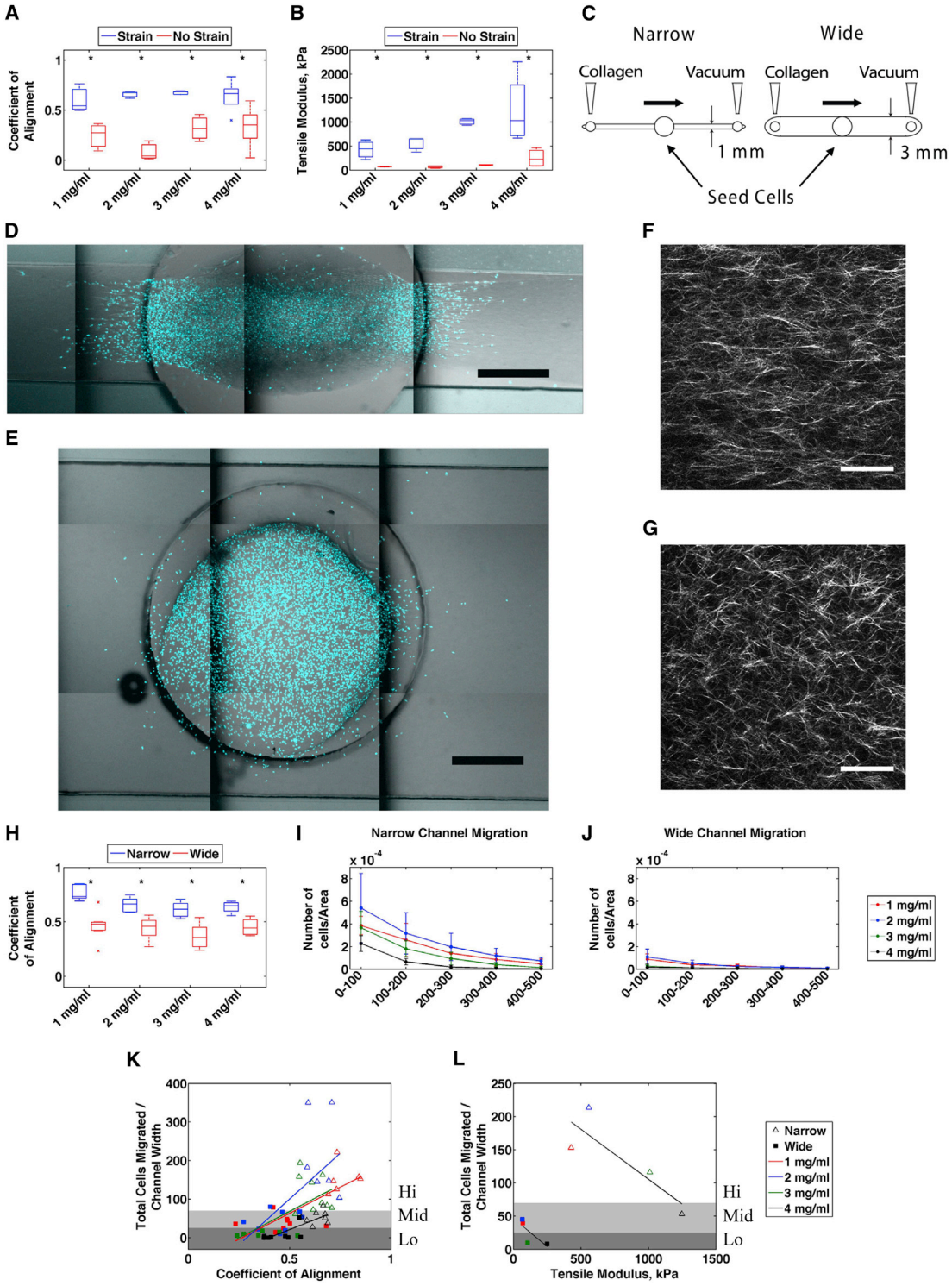

FIGURE 3 MDA-MB-231 cell migration is positively correlated with collagen alignment. (*A*) Coefficient of alignment of 1, 2, 3, and 4 mg/ml unstrained and 30% prestrained gels quantified using CurveAlign software ($n = 3$ gels, $p < 0.05$). (*B*) Tensile modulus of 1, 2, 3, and 4 mg/ml unstrained and 30% prestrained gels fixed with PFA ($n = 3$, $p < 0.05$). (*C*) Schematic depicting the microchannel migration assay. Flow of collagen through narrow channels results in alignment. (*D* and *E*) Representative confocal montages of narrow (*D*) and wide (*E*) channels, with cell nuclei stained with DAPI. Scale bar, 500 μm. (*F* and *G*) Representative SHG images of collagen in narrow (*F*) and wide (*G*) channels. Scale bar, 50 μm. (*H*) CurveAlign software analysis of coefficient of alignment in 1, 2, 3, and 4 mg/ml narrow and wide microchannels ($p < 0.01$). (*I* and *J*) Quantification of cell density outside of the channel port in concentric rings (100 μm wide) in narrow (*I*) and wide (*J*) channels ($n = 6$–9 channels). (*K* and *L*) Total cells that migrated normalized to the channel width is positively correlated with the coefficient of alignment (*K*) and inversely correlated with stiffness (*L*). Shaded regions represent statistical significance in migration and are designated as low (Lo), medium (Mid), and high (Hi) migration.

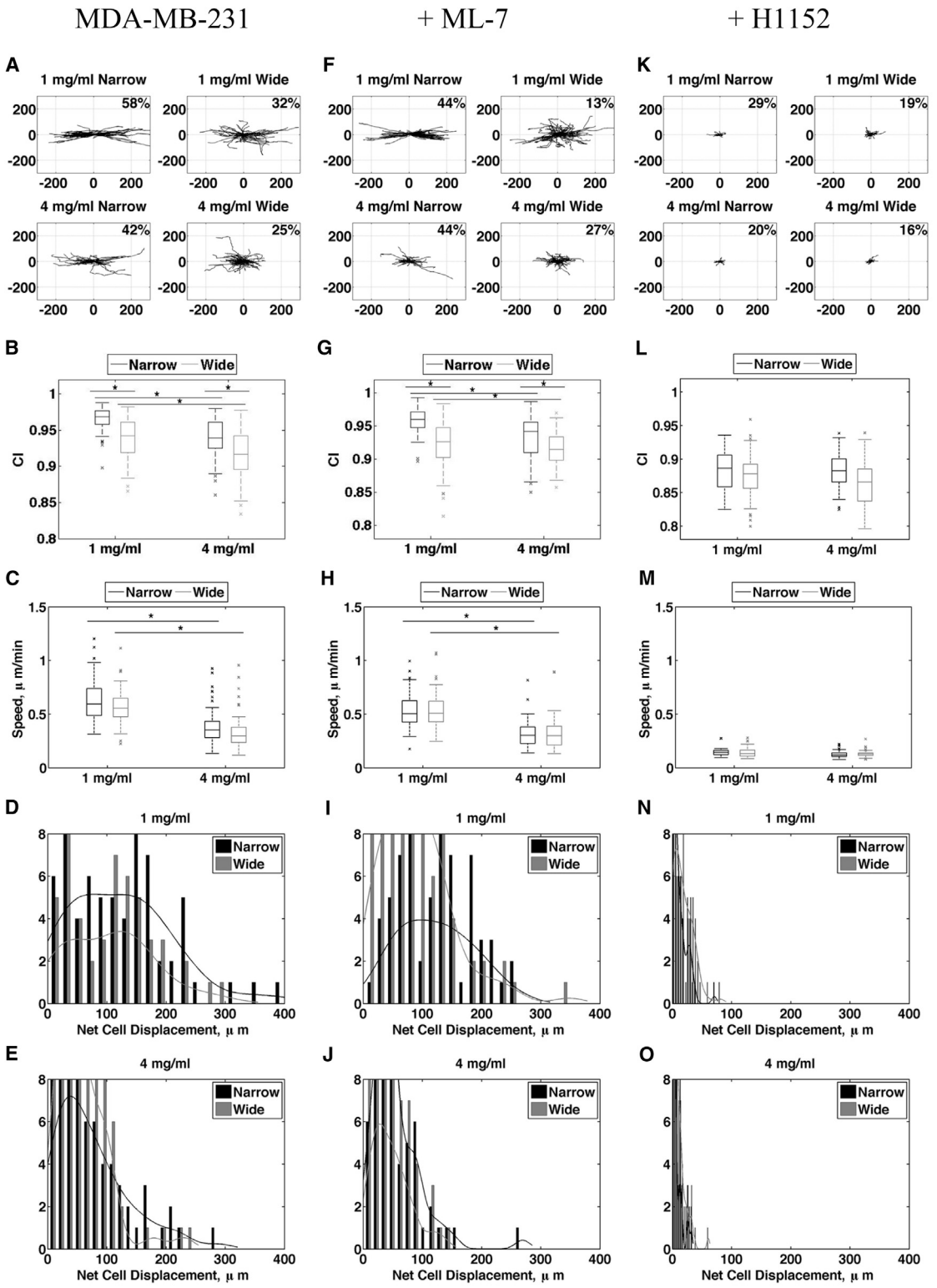

FIGURE 4 MDA-MB-231 cells migrate more slowly in stiff collagen and more directionally in aligned collagen. (*A*, *F*, and *K*) Windrose plots of all tracks analyzed during a 6 h confocal time lapse with a 10 min collection interval for untreated cells and cells treated with 2 μM ML-7 or 10 μM H1152 in narrow and wide channels (1 and 4 mg/ml). Percentages represent the fraction of cells with net track angles within 10° of the abscissa. (*B*, *G*, and *L*) Quantification of the CI for untreated and ML-7- and H1152-treated cells in narrow and wide channels (1 and 4 mg/ml, $p < 0.01$). (*C*, *H*, and *M*) Quantification of migration speed for untreated and ML-7- and H1152-treated cells in narrow and wide channels (1 and 4 mg/ml, $n > 40$, $p < 0.01$). (*D*, *E*, *I*, *J*, *N*, and *O*) Histograms of the cells' net displacements over 6 h in 1 and 4 mg/ml for untreated and ML-7- and H1152-treated cells.

To deduce a potential mechanism for cells' enhanced directional response to alignment, we asked whether Rho-mediated cell contractility plays a role in sensing alignment. We previously showed that cells require Rho and its effector, ROCK, to align collagen fibers, but once alignment is established, migration ensues independently of Rho and ROCK (23). To test whether cells require contractility to migrate in aligned collagen, we conducted time-lapse experiments similar to those shown in Fig. 4, *A–E*, but added to the culture media either H1152 to inhibit ROCK, or ML-7 to inhibit myosin light chain kinase (MLCK) 30 min before imaging. Inhibition of either ROCK or MLCK in MDA-MB-231 cells resulted in reduced levels of phosphorylated threonine-18 and serine-19 on MLC (data not shown), whereas ML-7 had no effect on migration speed or persistence compared with untreated cells (Fig. 4, *F–J*). However, H1152 dramatically inhibited cell speed across all conditions tested, which further resulted in reduced persistence (Fig. 4, *K–O*). These results indicate that Rho- and ROCK-mediated signaling is required for cell migration in 3D collagen matrices, but signaling from MLCK is not.

Our previous measurements of stiffness were at the bulk-material level and were aimed at assessing the relative moduli of ECM networks. However, individual cells experience the moduli of individual fibers in the network on a microscale. Therefore, to make more direct comparisons between matrix stiffness and the observed migration in microchannels, we measured the displacements of individual collagen fibers adjacent to migrating cells. Collagen was labeled with fluorescein isothiocyanate (FITC) according to Baici et al. (41), mixed with unlabeled collagen at a ratio of 1:10, and polymerized in narrow and wide microchannels. In this way, collagen fibers could be visualized by FITC immunofluorescence. FITC-collagen fibers and MDA-MB-231 cells seeded in the channels were imaged every 4 min for a period of 2 h by confocal microscopy. Time-lapse movies in 1 mg/ml narrow and wide channels were used to quantify cell-induced collagen fiber displacement (Movie S2). The fiber displacements measured in narrow channels were significantly smaller than those in wide channels for both 1 and 4 mg/ml conditions (Fig. 5 *A*), providing further support for the notion that aligned collagen, even at the cellular scale, is stiffer than a random matrix. Furthermore, the trends in fiber displacement in each condition correlate well with the trends in measured tensile moduli in Fig. 3 *B*, with the greatest fiber displacement occurring in the condition with the lowest measured bulk modulus, and vice versa. Similar fiber displacements were observed in both 1 mg/ml narrow and 4 mg/ml wide channels, which also have similar moduli (Fig. 3 *B*).

We next determined whether the inhibition of ROCK or MLCK affects fiber displacement in addition to migration. Consistent with the results shown in Fig. 5, inhibition of MLCK with ML-7 had no effect on total fiber displacement (Fig. 5 *B*), whereas inhibition of ROCK with H1152 reduced

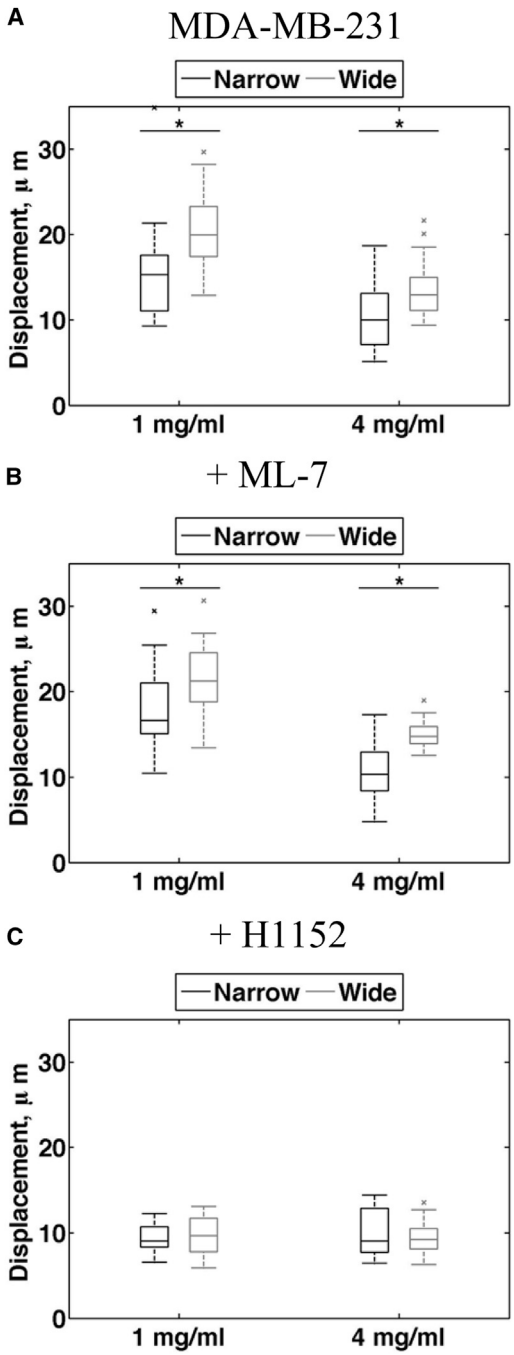

FIGURE 5 MDA-MB-231 cells displace collagen fibers in proportion to matrix stiffness. (*A–C*) Quantification of total collagen fiber displacement during a 2 h confocal time lapse with a 4 min collection interval for untreated and ML-7- and H1152-treated cells in narrow and wide channels (1 and 4 mg/ml, $n > 15$, $p < 0.001$).

fiber displacement in all conditions (Fig. 5 *C*). These results further suggest that ROCK, but not MLCK, is required for cells to displace the matrix and subsequently migrate.

These data suggest a complex interplay among alignment, stiffness, and ligand density in affecting cell migration. To better understand this interplay, we developed a simple

mathematical model to make qualitative assessments of motility given certain matrix properties, such as alignment, stiffness, and ligand density. Our aim was to address the inherent difficulty of changing a single matrix property without affecting another one, and to shed additional light on the findings discussed herein. Our model assumed that cell speed in 3D is a bimodal function of both modulus and ligand density. This assumption was based on experimental results obtained with collagen-coated 2D polyacrylamide gels in which the modulus was altered when the ligand density was held constant or in which the ligand density was altered while the modulus was held constant (Fig. 6, *A* and *B*). This bimodal relationship is consistent with other reports of 2D cell migration (38,39,42,43). Additionally, for simplicity, we modeled cell movements in 2D, since cell displacement in 3D was measured in the *x-y* plane by confocal microscopy. We computed cell displacements by assigning random protrusion vectors at discrete time steps for a total of 36 time steps, corresponding to the experimental conditions under which we observed migration every 10 min for 6 h (also a total of 36 time steps). We defined coefficients to describe ligand density, stiffness, and alignment, and used these coefficients to scale the relative magnitudes of the *x* and *y* components of the protrusion vectors. A vector sum of the protrusion vectors gave the cell's net displacement at that time point. Simulations of 100 cells were conducted in MATLAB (The MathWorks, Natick, MA) to make qualitative predictions of the trends in cell migration in 3D collagen environments within a known range of fiber alignments, ligand densities, and moduli. For further discussion about the model's assumptions and equations, see Supplemental Materials and Methods, Fig. S2 and Table S1.

From the simulations, we generated windrose plots of all cell simulations in 1 and 4 mg/ml aligned and random matrices, and found agreement in the distribution of tracks compared with experimental results (Fig. 6 *C*). Simulations showing the trends in cell speed, CI, and net displacement (Fig. 6, *D–G*) also correspond with the data in Fig. 4. To show trends in migration over a broader range of untested matrix conditions, we varied stiffness, ligand density, and alignment in the model, and found that migration speed was unaffected by changes in alignment (Fig. 6 *H*), consistent with the observed data. Increasing alignment, however,

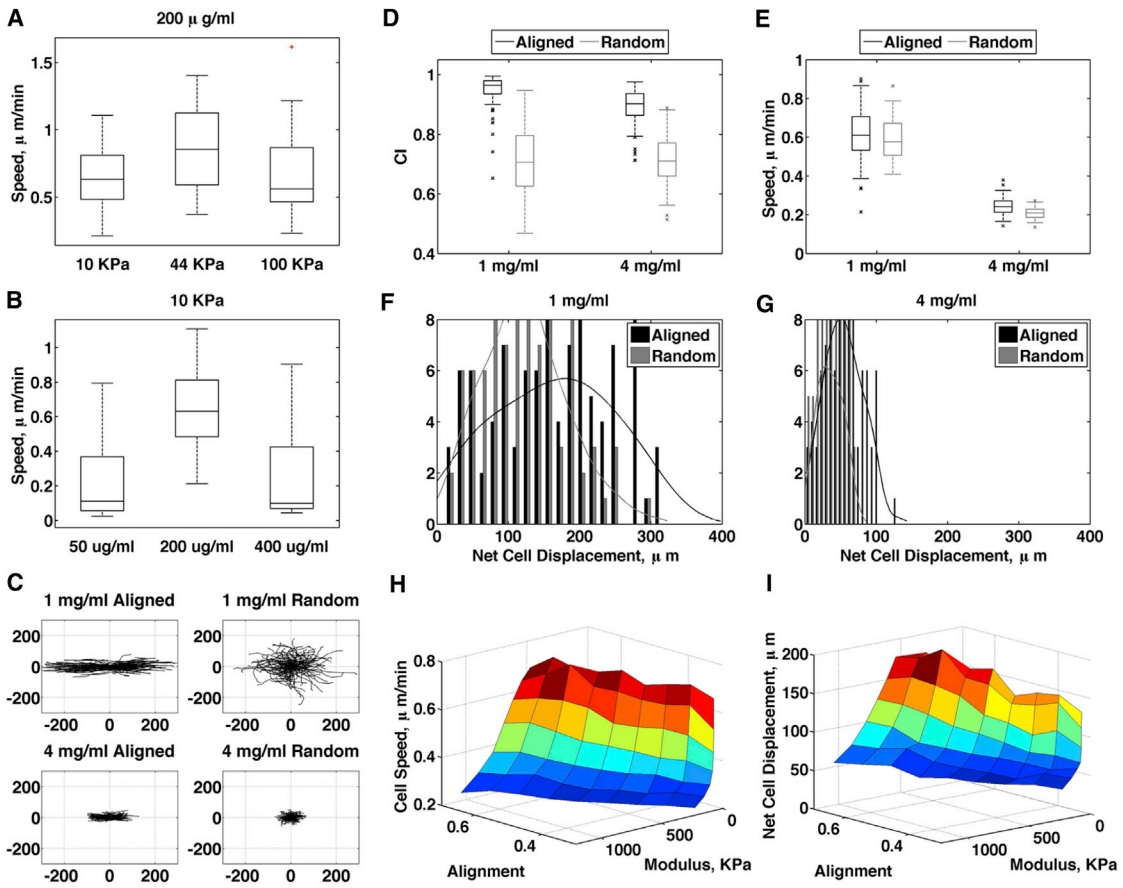

FIGURE 6 Computational model of cell migration replicates migration in 3D collagen. (*A* and *B*) 2D migration of MDA-MB-231 cells on polyacrylamide gels. (*C*) Windrose plots of simulated migration in 1 and 4 mg/ml aligned and random collagen from model. (*D* and *E*) Computed CI (*D*) and speed (*E*) from the model. (*F* and *G*) Histograms of computed cell displacements in 1 mg/ml (*F*) and 4 mg/ml (*G*) from the model. (*H* and *I*) Surface plot of cell speed (*H*) and net cell displacement (*I*) as a function of modulus and alignment.

increased the net distance cells traveled (Fig. 6 *I*), suggesting that an increase in persistence is the main factor that determines enhanced migration due to aligned collagen in invasive breast tumors. The model best fits the data when the number of protrusions per cell is decreased as alignment increases (Fig. S2 E), which leads to the prediction that alignment enhances persistence by limiting the number of protrusions.

To better understand the mechanism of enhanced persistence in aligned collagen, and to validate our model assumption that the number of protrusions changes with the organization of the matrix, we conducted time-lapse experiments to observe protrusion dynamics. To visualize actin-rich cellular protrusions, we generated stable MDA-MB-231 cells expressing Lifeact-mRFP, which was previously used to label filamentous actin in live cells (44). Confocal imaging showed that cells in aligned collagen elongated in the direction of alignment and with fewer peripheral protrusions compared with cells in a random matrix (Fig. 7 *A*). Time-lapse imaging also showed that elongated cells with prominent protrusions in the direction of alignment were maintained throughout the duration of the experiment, whereas cells in randomly organized collagen had less stable protrusions (Movie S3). In addition, we also observed in some cells the formation of membrane blebs similar to those previously associated with lobopodial migration 1D adhesive surfaces (45). We wrote and used custom MATLAB code to quantify the number and length of protrusions per cell at each time point (for further description, see Supplemental Materials and Methods). We found that cells in aligned collagen had fewer protrusions overall (Fig. 7 *B*), which is consistent with the prediction of the model. Moreover, as the model scaled the length of protrusions by the magnitude of the protrusion vector, our finding that the lengths of individual protrusions relative to the cell centroid were greater compared with those of cells cultured in randomly organized collagen (Fig. 7 *C*) is also consistent with the predictions of the model. These data indicate that aligned collagen restricts protrusions to the direction of alignment, potentially stabilizing protrusions in that direction and allowing cells to maintain greater persistence in aligned collagen.

DISCUSSION

Mammographic breast density and the accompanying stiffness are associated with increased breast cancer incidence (1,4,8), but do not correlate with distal relapse (46). In contrast, collagen alignment is associated with enhanced metastasis in animal models and poor prognosis in breast cancer patients (20,22). Despite the observation that migrating carcinoma cells track along collagen fibers in vitro and in vivo (20,47–49), the mechanism by which cells recognize and migrate along fibers is poorly understood. In this work, we sought to understand the effects of matrix stiffness and alignment on migrating epithelial cells within a 3D collagen matrix. We employed a coordinated analysis of both cell migration and tensile moduli of aligned and randomly organized matrices of varying stiffness. Consistent with our previous observations (23), we find that matrix alignment is a strong promoter of cell migration and results in a greater net distance traveled by cells. Surprisingly, matrix alignment does not enhance migration speed; rather, alignment enhances migrational persistence. Cells in aligned collagen have fewer and longer protrusions that are oriented with respect to aligned fibers, suggesting that limiting protrusions is the mechanism by which alignment serves to increase persistence.

Although it is well known that collagen exhibits strain-stiffening behavior, it is less understood how migrating cells

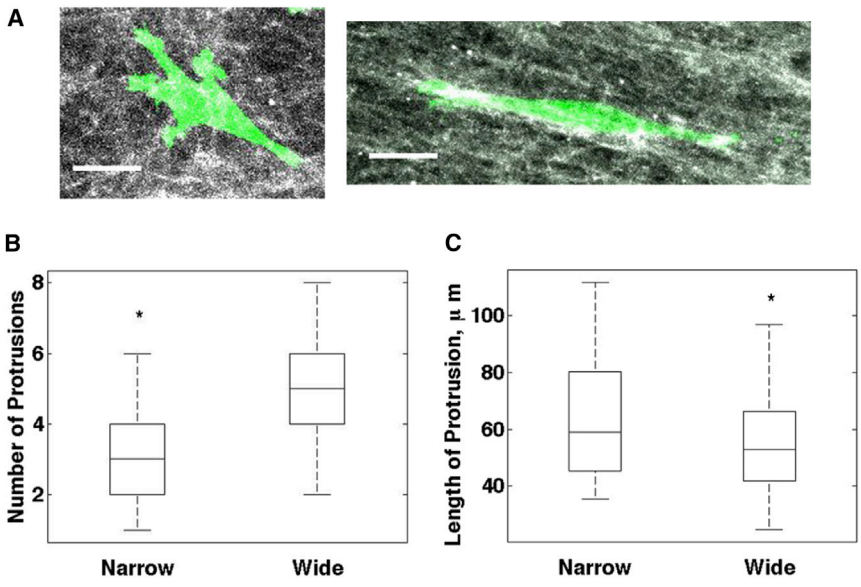

FIGURE 7 Cells in aligned collagen have fewer and longer protrusions. (*A*) Confocal z-compressed images of MDA-MB-231 cells expressing Lifeact-mRFP in 1 mg/ml wide (*left*) and narrow (*right*) channels. Grayscale, FITC-labeled collagen; green, Lifeact-mRFP. Scale bar: 20 μm. (*B* and *C*) Quantification of the number of protrusions per cell (*B*) and length of protrusion (*C*) relative to centroid ($n = 8$ cells, $p < 0.0001$).

respond to matrices of different fiber orientations and stiffness. Therefore, we characterized the mechanical effects of prestraining a collagen matrix to induce fiber alignment. Our results show that collagen prealigned by strain is stiffer than a random collagen matrix of the same density and that the stiffness is greatest along the axis of alignment. Xu et al. (50) previously conducted biaxial tensile testing of collagen prealigned by flow of magnetic beads and showed that after fixation, gels aligned parallel to the direction of alignment were stiffer than gels aligned orthogonally. Here, we obtained similar findings utilizing uniaxial tensile testing and a simpler, more robust approach to induce prealignment by strain rather than flow of magnetic beads embedded in the matrix. Moreover, we found that the increased stiffness of aligned gels is preserved even in unfixed collagen gels.

Our results further suggest that alignment of collagen fibers potentially strengthens and stabilizes interactions between neighboring fibers, presumably causing the observed increase in modulus. The act of stretching a collagen matrix not only results in increased fiber proximity but can also increase subfibrillar orientation and packing (51). These stretch-induced modifications may allow for enhanced molecular interactions between adjacent fibrils (52), thus increasing the overall matrix stiffness. Similarly, we expect that the flow-induced fiber alignment in our microchannels potentially enhances interactions between adjacent fibers such that alignment, rather than the method by which the alignment is induced, is the key feature.

To study cell migration in aligned matrices, we developed an assay that makes use of the observation made by Lee et al. (36) and Sung et al. (37) that collagen alignment can be controlled by flow through a sufficiently narrow microchannel. To our knowledge, this assay represents a novel approach for studying the effects of 3D collagen alignment on cell migration. Here, we used channels 1 mm and 3 mm wide to produce highly aligned collagen matrices and a randomly organized matrix, respectively, into which we seeded cells and quantified total cell migration, speed, and persistence. We found that more cells migrated farther into the aligned collagen, but migration speed was unchanged relative to migration in the randomly organized collagen matrix.

The increase in the total number of migrating cells in the aligned matrix can be accounted for by the marked increase in the persistence of cells in aligned collagen. Furthermore, our results demonstrate that the effects of collagen alignment on persistence are not due to the increased stiffness of an aligned matrix, or durotaxis, because cells migrated faster and were more persistent in 1 mg/ml aligned collagen than in 4 mg/ml random matrix, even though the two conditions had nearly the same stiffness. In contrast, we found that when increased matrix stiffness was generated by increased collagen concentration, which also increased the ligand density and reduced the porosity of the matrix, cell speed was reduced. This result is in contrast to the well-documented durotactic response of cells cultured on 2D substrates (14) and may reflect the greater inherent complexity of 3D matrices. Importantly, the mechanical properties extrapolated from measurements of fiber displacement correlate well with the measured bulk tensile moduli of aligned and random gels, suggesting that the differences in the mechanical properties of aligned and random collagen gels at the microscale correlate to the macroscale. Moreover, this finding demonstrates that increased stiffness along the axis of alignment is observed regardless of the mechanism of alignment (flow or strain).

We further show that migration is dependent on Rho/ROCK-generated contractility and independent of MLCK. Previously, we demonstrated that cells first require a contractile mechanism involving Rho and ROCK to generate aligned collagen, and that the requirement for Rho/ROCK ceases for migration in a prealigned collagen matrix (23). One possible explanation for this discrepancy is the difference in the duration of inhibitor treatment between the two studies (8 h in this study compared with every 24 h for a period of 3 days in the previous study), suggesting that compensation for Rho inhibition may occur over longer treatment time frames. As in our previous study, we again find that fiber displacement is also dependent on ROCK, not MLCK, which agrees with other reports of matrix deformation by contractile forces (53–55). These results provide additional support for the idea proposed by Grinnell et al. (56) and Miron-Mendoza et al. (57) that cell migration and matrix deformation are both consequences of the same Rho- and ROCK-driven contractile mechanism and could occur in concert. Matrix stiffness likely determines the extent of fiber deformation as well as the amount of traction a migrating cell can generate by utilizing Rho-mediated contractility.

From our results, we infer that the collagen fibers that are most constrained in the matrix move the least when pulled and exhibit the greatest stiffness. This finding is also supported by the observation of Lopez-Garcia et al. (58) that NMuMG cells produce larger strains in matrices of lower stiffness. These results lead to the assumption that stiffer conditions may provide the most traction and thus allow cells to use their contractile forces to achieve the fastest migration. Consistent with this idea, previous studies showed that stiffness increases the amount of force adhesions generate, and force-generating active Rho is upregulated in stiff matrices (10,53,59). These findings on their own would predict that increased stiffness in 3D would lead to enhanced migration speeds. However, increasing stiffness in 3D matrices is also typically accompanied by increased ligand density and decreased matrix porosity, both of which are known to significantly impact migration speed (39,40). For this reason, it has often been challenging to develop techniques that allow one to separate stiffness from other factors in a 3D environment to assess changes in migratory behavior. Recently, however, Harley et al.

(60) were able to alter the individual strut stiffness of a collagen-GAG scaffold, and identified a bimodal relationship between stiffness and cell migration speed similar to that seen on 2D substrates. As new methods for engineering matrices with precisely controlled physical and mechanical properties become available, we will be able to study additional relationships involving cell speed and persistence.

To address the multifactorial responses to the topographical and mechanical properties of the matrix, we developed a mathematical model that incorporates matrix ligand density, stiffness, and alignment. Our model allows us to better understand the trends over the range of experimental conditions tested, where it is difficult to deduce effects incurred by isolating a single 3D matrix parameter. Others have proposed a model to describe the effect of fibroblast migration speed on the alignment of fibrin and collagen in dermal wound healing (61). Our model considers protrusion generation as a stochastic process that leads to adhesion formation with ECM fibers, whereas other groups have used models to suggest that in vivo migration in discontinuous environments may not require adhesions (62). Our model predicts that the number of protrusions diminish with increased alignment and increase as ligand density increases. We show experimentally that cells in aligned collagen indeed have fewer protrusions, which is likely responsible for this observed increase in persistence. To better replicate cell persistence, the model incorporates a probability for a protrusion vector to maintain its orientation across multiple time steps that increases as a function of matrix alignment. Although we are unsure of the exact cellular mechanism of persistence, the predictions of our model would be consistent with the hypothesis that persistence reflects the presentation of ligands along an axis allowing cells to form and stabilize adhesions in a given direction, enabling more efficient migration. This notion is consistent with the observation that integrin adhesions are localized along collagen fibers in 3D (63) and on 1D collagen fibers, where cell migration along 1D fibers recapitulates migration in 3D matrices (64). Moreover, we expect that persistence also reflects the loss of competing ligand binding choices in other directions. We predict that as ligand concentration increases, there will be more opportunities for adhesion-stabilized protrusions to occur outside the direction of alignment, consistent with the observation that persistence decreases as ligand concentration increases.

A limitation of our model is that, for simplicity, it assumes all matrix parameters are held constant over the simulated time frame, when in reality cells are constantly modifying their environment via Rho/ROCK contractility, which causes local changes in alignment, stiffness, and ligand density. Moreover, there are additional effects of proteolytic modification of collagen that we have not taken into account (63). Furthermore, the model input parameters require tested modulus values for given alignments and ligand densities, which can also change with different matrix components and the extent of cross-linking. Once we are able to measure the stiffness of a broader range of matrix compositions and more reliably establish the relationships among matrix composition, alignment, and stiffness, we can revise the model parameters. Despite these limitations, however, we show that our model can accurately replicate trends in migration speed and persistence in 1 mg/ml and 4 mg/ml aligned and random collagen matrices. Furthermore, the model is consistent with the observation that migration speed across a range of matrix conditions is unaffected by alignment, but alignment profoundly increases the net distance cells travel. This finding is significant in the context of breast tumor progression, where the presence of TACS-3 aligned fibers is correlated with a dramatic increase in metastases and poor long-term survival (21,22). Our results suggest that highly aligned regions in the tumor microenvironment can provide cells that have a high migratory capacity with the most reliable and robust escape route, and provide additional mechanistic understanding of how the aligned collagen characterized by TACS-3 relates to its role as a potential biomarker for breast cancer.

SUPPORTING MATERIAL

Supplemental Materials and Methods, three figures, one table, and three movies are available at http://www.biophysj.org/biophysj/supplemental/S0006-3495(14)01118-7.

The authors thank Drs. Kyung Sung and David Beebe for assistance with microfluidic channels, Dr. Maddy Parsons for generously supplying the Lifeact-mRFP construct, and Curtis Rueden for assistance with the FIJI software and analysis.

This work was funded by NIH grants U01CA143069 to A.W., Y.J., and P.J.K., and R01 CA142833 and R01 CA114462 to P.J.K. and supported by the University of Wisconsin-Madison Graduate School for M.R.S. and W.C.C.

SUPPORTING CITATIONS

References (65–74) appear in the Supporting Material.

REFERENCES

1. Boyd, N. F., G. A. Lockwood, …, M. J. Yaffe. 1998. Mammographic densities and breast cancer risk. *Cancer Epidemiol. Biomarkers Prev.* 7:1133–1144.

2. Boyd, N. F., L. J. Martin, …, M. J. Yaffe. 2001. Mammographic densities as a marker of human breast cancer risk and their use in chemoprevention. *Curr. Oncol. Rep.* 3:314–321.

3. McCormack, V. A., and I. dos Santos Silva. 2006. Breast density and parenchymal patterns as markers of breast cancer risk: a meta-analysis. *Cancer Epidemiol. Biomarkers Prev.* 15:1159–1169.

4. Boyd, N. F., G. S. Dite, …, J. L. Hopper. 2002. Heritability of mammographic density, a risk factor for breast cancer. *N. Engl. J. Med.* 347:886–894.

5. Alowami, S., S. Troup, …, P. H. Watson. 2003. Mammographic density is related to stroma and stromal proteoglycan expression. *Breast Cancer Res.* 5:R129–R135.

6. Li, T., L. Sun, …, N. Boyd. 2005. The association of measured breast tissue characteristics with mammographic density and other risk factors for breast cancer. *Cancer Epidemiol. Biomarkers Prev.* 14:343–349.

7. Guo, Y. P., L. J. Martin, …, N. F. Boyd. 2001. Growth factors and stromal matrix proteins associated with mammographic densities. *Cancer Epidemiol. Biomarkers Prev.* 10:243–248.

8. Paszek, M. J., N. Zahir, …, V. M. Weaver. 2005. Tensional homeostasis and the malignant phenotype. *Cancer Cell.* 8:241–254.

9. Lopez, J. I., I. Kang, …, V. M. Weaver. 2011. In situ force mapping of mammary gland transformation. *Integr. Biol.* (*Camb.*). 3:910–921.

10. Provenzano, P. P., D. R. Inman, …, P. J. Keely. 2009. Matrix density-induced mechanoregulation of breast cell phenotype, signaling and gene expression through a FAK-ERK linkage. *Oncogene.* 28:4326–4343.

11. Tilghman, R. W., C. R. Cowan, …, J. T. Parsons. 2010. Matrix rigidity regulates cancer cell growth and cellular phenotype. *PLoS ONE.* 5:e12905.

12. Alexander, N. R., K. M. Branch, …, A. M. Weaver. 2008. Extracellular matrix rigidity promotes invadopodia activity. *Curr. Biol.* 18:1295–1299.

13. Lo, C. M., H. B. Wang, …, Y. L. Wang. 2000. Cell movement is guided by the rigidity of the substrate. *Biophys. J.* 79:144–152.

14. Pelham, Jr., R. J., and Yl. Wang. 1997. Cell locomotion and focal adhesions are regulated by substrate flexibility. *Proc. Natl. Acad. Sci. USA.* 94:13661–13665.

15. Menon, S., and K. A. Beningo. 2011. Cancer cell invasion is enhanced by applied mechanical stimulation. *PLoS ONE.* 6:e17277.

16. Kostic, A., C. D. Lynch, and M. P. Sheetz. 2009. Differential matrix rigidity response in breast cancer cell lines correlates with the tissue tropism. *PLoS ONE.* 4:e6361.

17. Wozniak, M. A., K. Modzelewska, …, P. J. Keely. 2004. Focal adhesion regulation of cell behavior. *Biochim. Biophys. Acta.* 1692:103–119.

18. Klein, E. A., L. Yin, …, R. K. Assoian. 2009. Cell-cycle control by physiological matrix elasticity and in vivo tissue stiffening. *Curr. Biol.* 19:1511–1518.

19. Ulrich, T. A., E. M. de Juan Pardo, and S. Kumar. 2009. The mechanical rigidity of the extracellular matrix regulates the structure, motility, and proliferation of glioma cells. *Cancer Res.* 69:4167–4174.

20. Provenzano, P. P., K. W. Eliceiri, …, P. J. Keely. 2006. Collagen reorganization at the tumor-stromal interface facilitates local invasion. *BMC Med.* 4:38.

21. Provenzano, P. P., D. R. Inman, …, P. J. Keely. 2008. Collagen density promotes mammary tumor initiation and progression. *BMC Med.* 6:11.

22. Conklin, M. W., J. C. Eickhoff, …, P. J. Keely. 2011. Aligned collagen is a prognostic signature for survival in human breast carcinoma. *Am. J. Pathol.* 178:1221–1232.

23. Provenzano, P. P., D. R. Inman, …, P. J. Keely. 2008. Contact guidance mediated three-dimensional cell migration is regulated by Rho/ROCK-dependent matrix reorganization. *Biophys. J.* 95:5374–5384.

24. Kim, A., N. Lakshman, and W. M. Petroll. 2006. Quantitative assessment of local collagen matrix remodeling in 3-D culture: the role of Rho kinase. *Exp. Cell Res.* 312:3683–3692.

25. Brownfield, D. G., G. Venugopalan, …, M. J. Bissell. 2013. Patterned collagen fibers orient branching mammary epithelium through distinct signaling modules. *Curr. Biol.* 23:703–709.

26. Sander, E. A., V. H. Barocas, and R. T. Tranquillo. 2011. Initial fiber alignment pattern alters extracellular matrix synthesis in fibroblast-populated fibrin gel cruciforms and correlates with predicted tension. *Ann. Biomed. Eng.* 39:714–729.

27. Wang, J. H., F. Jia, …, S. L. Woo. 2003. Cell orientation determines the alignment of cell-produced collagenous matrix. *J. Biomech.* 36:97–102.

28. Yang, N., R. Mosher, …, A. Friedl. 2011. Syndecan-1 in breast cancer stroma fibroblasts regulates extracellular matrix fiber organization and carcinoma cell motility. *Am. J. Pathol.* 178:325–335.

29. Gruschwitz, R., J. Friedrichs, …, K. Engelmann. 2010. Alignment and cell-matrix interactions of human corneal endothelial cells on nanostructured collagen type I matrices. *Invest. Ophthalmol. Vis. Sci.* 51:6303–6310.

30. Vernon, R. B., M. D. Gooden, …, T. N. Wight. 2005. Microgrooved fibrillar collagen membranes as scaffolds for cell support and alignment. *Biomaterials.* 26:3131–3140.

31. Kim, D. H., P. P. Provenzano, …, A. Levchenko. 2012. Matrix nanotopography as a regulator of cell function. *J. Cell Biol.* 197:351–360.

32. Lai, E. S., N. F. Huang, …, G. G. Fuller. 2012. Aligned nanofibrillar collagen regulates endothelial organization and migration. *Regen. Med.* 7:649–661.

33. Friedl, P., and K. Wolf. 2008. Tube travel: the role of proteases in individual and collective cancer cell invasion. *Cancer Res.* 68:7247–7249.

34. Vader, D., A. Kabla, …, L. Mahadevan. 2009. Strain-induced alignment in collagen gels. *PLoS ONE.* 4:e5902.

35. Roeder, B. A., K. Kokini, …, S. L. Voytik-Harbin. 2002. Tensile mechanical properties of three-dimensional type I collagen extracellular matrices with varied microstructure. *J. Biomech. Eng.* 124:214–222.

36. Lee, P., R. Lin, …, L. P. Lee. 2006. Microfluidic alignment of collagen fibers for in vitro cell culture. *Biomed. Microdevices.* 8:35–41.

37. Sung, K. E., G. Su, …, D. J. Beebe. 2009. Control of 3-dimensional collagen matrix polymerization for reproducible human mammary fibroblast cell culture in microfluidic devices. *Biomaterials.* 30:4833–4841.

38. Palecek, S. P., J. C. Loftus, …, A. F. Horwitz. 1997. Integrin-ligand binding properties govern cell migration speed through cell-substratum adhesiveness. *Nature.* 385:537–540.

39. Zaman, M. H., L. M. Trapani, …, P. Matsudaira. 2006. Migration of tumor cells in 3D matrices is governed by matrix stiffness along with cell-matrix adhesion and proteolysis. *Proc. Natl. Acad. Sci. USA.* 103:10889–10894.

40. Wolf, K., M. Te Lindert, …, P. Friedl. 2013. Physical limits of cell migration: control by ECM space and nuclear deformation and tuning by proteolysis and traction force. *J. Cell Biol.* 201:1069–1084.

41. Baici, A., G. Cohen, …, A. Böni. 1980. A handy assay for collagenase using reconstituted fluorescein-labeled collagen fibrils. *Anal. Biochem.* 108:230–232.

42. Wu, P., J. B. Hoying, …, D. A. Lauffenburger. 1994. Integrin-binding peptide in solution inhibits or enhances endothelial cell migration, predictably from cell adhesion. *Ann. Biomed. Eng.* 22:144–152.

43. Peyton, S. R., and A. J. Putnam. 2005. Extracellular matrix rigidity governs smooth muscle cell motility in a biphasic fashion. *J. Cell. Physiol.* 204:198–209.

44. Riedl, J., A. H. Crevenna, …, R. Wedlich-Soldner. 2008. Lifeact: a versatile marker to visualize F-actin. *Nat. Methods.* 5:605–607.

45. Petrie, R. J., N. Gavara, …, K. M. Yamada. 2012. Nonpolarized signaling reveals two distinct modes of 3D cell migration. *J. Cell Biol.* 197:439–455.

46. Park, C. C., J. Rembert, …, K. Kerlikowske. 2009. High mammographic breast density is independent predictor of local but not distant recurrence after lumpectomy and radiotherapy for invasive breast cancer. *Int. J. Radiat. Oncol. Biol. Phys.* 73:75–79.

47. Wang, W., J. B. Wyckoff, …, J. S. Condeelis. 2002. Single cell behavior in metastatic primary mammary tumors correlated with gene expression patterns revealed by molecular profiling. *Cancer Res.* 62:6278–6288.

48. Dickinson, R. B., S. Guido, and R. T. Tranquillo. 1994. Biased cell migration of fibroblasts exhibiting contact guidance in oriented collagen gels. *Ann. Biomed. Eng.* 22:342–356.

49. Petrie, R. J., A. D. Doyle, and K. M. Yamada. 2009. Random versus directionally persistent cell migration. *Nat. Rev. Mol. Cell Biol.* 10:538–549.

50. Xu, B., M. J. Chow, and Y. Zhang. 2011. Experimental and modeling study of collagen scaffolds with the effects of crosslinking and fiber alignment. *Int. J. Biomater.* 2011:172389.

51. Pins, G. D., D. L. Christiansen, …, F. H. Silver. 1997. Self-assembly of collagen fibers. Influence of fibrillar alignment and decorin on mechanical properties. *Biophys. J.* 73:2164–2172.

52. Freeman, J. W., and F. H. Silver. 2005. The effects of prestrain and collagen fibril alignment on in vitro mineralization of self-assembled collagen fibers. *Connect. Tissue Res.* 46:107–115.

53. Wozniak, M. A., R. Desai, …, P. J. Keely. 2003. ROCK-generated contractility regulates breast epithelial cell differentiation in response to the physical properties of a three-dimensional collagen matrix. *J. Cell Biol.* 163:583–595.

54. Wyckoff, J. B., S. E. Pinner, S. Gschmeissner, J. S. Condeelis, and E. Sahai. 2006. ROCK- and myosin-dependent matrix deformation enables protease-independent tumor-cell invasion in vivo. *Curr. Biol.* Aug 8; 16(15):1515–1523.

55. Lakshman, N., A. Kim, …, W. M. Petroll. 2007. Rho plays a central role in regulating local cell-matrix mechanical interactions in 3D culture. *Cell Motil. Cytoskeleton.* 64:434–445.

56. Grinnell, F., L. B. Rocha, …, H. Jiang. 2006. Nested collagen matrices: a new model to study migration of human fibroblast populations in three dimensions. *Exp. Cell Res.* 312:86–94.

57. Miron-Mendoza, M., J. Seemann, and F. Grinnell. 2008. Collagen fibril flow and tissue translocation coupled to fibroblast migration in 3D collagen matrices. *Mol. Biol. Cell.* 19:2051–2058.

58. Lopez-Garcia, M. D., D. J. Beebe, and W. C. Crone. 2010. Mechanical interactions of mouse mammary gland cells with collagen in a three-dimensional construct. *Ann. Biomed. Eng.* 38:2485–2498.

59. Bhadriraju, K., M. Yang, …, C. S. Chen. 2007. Activation of ROCK by RhoA is regulated by cell adhesion, shape, and cytoskeletal tension. *Exp. Cell Res.* 313:3616–3623.

60. Harley, B. A., H. D. Kim, …, L. J. Gibson. 2008. Microarchitecture of three-dimensional scaffolds influences cell migration behavior via junction interactions. *Biophys. J.* 95:4013–4024.

61. Dallon, J. C., J. A. Sherratt, and P. K. Maini. 2001. Modeling the effects of transforming growth factor-beta on extracellular matrix alignment in dermal wound repair. *Wound Repair Regen.* 9:278–286.

62. Tozluoğlu, M., A. L. Tournier, …, E. Sahai. 2013. Matrix geometry determines optimal cancer cell migration strategy and modulates response to interventions. *Nat. Cell Biol.* 15:751–762.

63. Wolf, K., Y. I. Wu, …, P. Friedl. 2007. Multi-step pericellular proteolysis controls the transition from individual to collective cancer cell invasion. *Nat. Cell Biol.* 9:893–904.

64. Doyle, A. D., F. W. Wang, …, K. M. Yamada. 2009. One-dimensional topography underlies three-dimensional fibrillar cell migration. *J. Cell Biol.* 184:481–490.

65. Heck, J. N., S. M. Ponik, …, P. J. Keely. 2012. Microtubules regulate GEF-H1 in response to extracellular matrix stiffness. *Mol. Biol. Cell.* 23:2583–2592.

66. Chua Chee, K. 1994. Three-dimensional rapid prototyping technologies and key development areas. *Comput. Contr. Eng. J.* 5:200–206.

67. Wozniak, M. A., and P. J. Keely. 2005. Use of three-dimensional collagen gels to study mechanotransduction in T47D breast epithelial cells. *Biol. Proced. Online.* 7:144–161.

68. Lopez-Garcia, M. D., D. J. Beebe, and W. C. Crone. 2010. Young's modulus of collagen at slow displacement rates. *Biomed. Mater. Eng.* 20:361–369.

69. Schindelin, J., I. Arganda-Carreras, …, A. Cardona. 2012. Fiji: an open-source platform for biological-image analysis. *Nat. Methods.* 9:676–682.

70. Yeung, T., P. C. Georges, …, P. A. Janmey. 2005. Effects of substrate stiffness on cell morphology, cytoskeletal structure, and adhesion. *Cell Motil. Cytoskeleton.* 60:24–34.

71. Aratyn-Schaus, Y., P. W. Oakes, …, M. L. Gardel. 2010. Preparation of complaint matrices for quantifying cellular contraction. *J. Vis. Exp.* (46): pii: 2173.

72. Schoen, I., B. L. Pruitt, and V. Vogel. 2013. The yin-yang of rigidity sensing: how forces and mechanical properties regulate the cellular response to materials. *Annu. Rev. Mater. Res.* 43:589–618.

73. Smith, A. S., K. Sengupta, …, E. Sackmann. 2008. Force-induced growth of adhesion domains is controlled by receptor mobility. *Proc. Natl. Acad. Sci. USA.* 105:6906–6911.

74. Huttenlocher, A., and A. R. Horwitz. 2011. Integrins in cell migration. *Cold Spring Harb. Perspect. Biol.* 3:a005074.

Kristin M. Riching,[†‡] Benjamin Cox,[§] Max R. Salick,[¶||] Carolyn Pehlke,[‡] Andrew S. Riching,[**] Benjamin R. Bass,[††] Wendy C. Crone,[||] Yi Jiang,[‡‡] Alissa Weaver, [§§] Kevin W. Eliceiri, [‡†§¶¶] and Patricia J. Keely[‡¶¶||||*]

3D collagen alignment enhances breast cancer cell persistence and limits protrusions

SUPPLEMENTARY MATERIAL

This file contains the following items:

1. Supplementary Materials and Methods
2. Supplementary legends for Movies S1, S2, and S3
3. Supplementary Figure S1, Figure S2, and Figure S3
4. Supplementary Table S1

[†] Biomedical Engineering Program, University of Wisconsin, Madison, Wisconsin 53706,
[‡] Laboratory for Optical and Computational Instrumentation, University of Wisconsin, Madison, Wisconsin 53706,
[§] Department of Medical Physics, University of Wisconsin, Madison, Wisconsin 53706,
[¶] Materials Science Program, University of Wisconsin, Madison, Wisconsin 53706,
[||] Department of Engineering Physics, University of Wisconsin, Madison, Wisconsin 53706,
[**] Department of Cell and Regenerative Biology, University of Wisconsin, Madison, Wisconsin 53706
[††] Saris Cycling Group, Madison, Wisconsin, 53711,
[‡‡] Department of Mathematics and Statistics, Georgia State University, Atlanta, Georgia 30303,
[§§] Department of Cancer Biology, Vanderbilt University Medical Center, Nashville, Tennessee 37232,
[¶¶] Department of Cell and Regenerative Biology, University of Wisconsin, Madison, Wisconsin 53706, and
[||||] University of Wisconsin Paul P. Carbone Comprehensive Cancer Center, University of Wisconsin, Madison, Wisconsin 53706,

Supplementary Materials and Methods

Reagents and chemicals

Type I rat tail collagen was obtained from BD Biosciences (San Jose, CA). DMEM cell culture media was purchased from Life Technologies (Grand Island, NY) and fetal bovine serum was purchased from Gemini Bio-Products (West Sacramento, CA). MDA-MB-231 epithelial cells were obtained from ATCC (Manassas, VA). Phospho-MLC antibody was purchased from Cell Signaling Technology (Danvers, MA). The ROCK inhibitor H1152 and the MLCK inhibitor ML-7 were purchased from EMD Millipore (Darmstadt, Germany).

Cell culture and transfection

MDA-MB-231 cells were maintained in DMEM with 10% serum in a 37°C incubator with 5% CO_2. Lentiviral Lifeact-mRFP constructs were a kind gift from Maddy Parsons (King's College London, London, UK). Phoenix (HEK293) cells were obtained from the National Gene Vectro Biorepository (Indianapolis, IN) and used for lentiviral production as described (1). Cells were removed from culture dishes with 0.05% trypsin and centrifuged at 300 × *g* for 3 min to remove trypsin prior to addition of neutralized collagen solution for culture in 3D collagen gels.

Mechanical alignment of collagen gels

A device to mechanically strain dogbone-shaped collagen gels was modeled in SolidWorks (Daussalt Systemes, Waltham, MA) and 3D-printed. The device was based on a design by Vader et al. (2), and consisted of a micrometer that drove and accurately recorded displacements of one of two pins that contacted pieces of polypropylene mesh embedded in the gel. The device was mounted to a 3D printed stage designed to fit a multiphoton microscope. Dogbone-shaped collagen gels were pre-strained to 30% using this strain device prior to mechanical testing and were either left unfixed or were fixed with 4% paraformaldehyde for 10 minutes.

To strain larger collagen dogbone-shaped specimens, a weight-based loading system was used. This system consisted of a set of grips where one grip remained stationary and the other was pulled horizontally by a cable attached to a series of weights hung over a pulley. Both grips containing the collagen gel were immersed in a bath of PBS and the gel was strained to 30%, after which the gel was fixed with 4% paraformaldehyde for 10 minutes. The gel was then removed from the grips and a 3D-printed cutter in the shape of a dogbone was used to cut specimens either parallel or perpendicular to the direction of the applied strain. Grip sections of the cut specimens were carefully sandwiched between pieces of polypropylene mesh to facilitate handling.

3D printing

Several components of the collagen strain device were fabricated using three-dimensional (3D) printing techniques. The stage of the strain device was made using a Dimension Elite 3D Printer (Stratasys Ltd., Rehovot, Israel). This machine creates plastic parts using the process of fused deposition modeling (FDM). The arm that held the stationary pin and the arm that connected to the micrometer in the strain device were fabricated using a Viper Si2 3D Printer (3D Systems inc., Rock Hill, SC). This machine creates parts using the process of stereolithography (SL). Both of these processes have been previously described (3).

Mechanical testing of collagen

Collagen gels were prepared by neutralizing acid-soluble rat-tail collagen with 100mM HEPES buffer in 2x PBS in a 1:1 ratio, and then diluted with DMEM to obtain the final collagen concentration as described in Wozniak et al. (4). Neutralized collagen was then poured into a stainless steel mold in the shape of a dogbone with dimensions taken from Roeder et al. (5). These dimensions consisted of a 10mm long by 4mm wide and approximately 1mm thick gauge region, and 10mm long by 20mm wide grip sections. Pieces of polypropylene mesh were embedded into the grip sections of the dogbone to facilitate removal from the mold and to ensure adequate sample gripping for mechanical testing. Gels were left undisturbed at room temperature until gels were visibly opaque, then stored in a 37°C incubator to complete polymerization overnight. The cross-sectional area of the dogbone gauge region was measured using digital calipers to measure the width, and optical sectioning by second harmonic imaging and a 10x objective to measure gel thickness. Tensile testing was performed using a similar procedure as Lopez-Garcia et al. (6). Briefly, a vertical-loading Instron 5548 MicroTester with a 10 N load cell and a crosshead displacement rate of 1mm/min was used. Samples loaded into the grips of the Instron were then immersed in a PBS-filled custom water-jacketed Pyrex environmental chamber heated to 37°C with a PolyScience digital temperature controller heater/circulator for the duration of the test. Load data was acquired using Merlin v5.04 software. 1μm glass beads were deposited on the surface of collagen specimens and imaged every 10 seconds using a Photometrics MicroPublisher 5.0 RTV and QCapture Pro 5.1.1.14 acquisition software. All samples were strained until failure, and samples where failure occurred prematurely at the grip sections were discarded. The effect of buoyancy on the load cell was measured by conducting an identical test without the specimen for all measured specimens, and subtracted from the data to obtain the load incurred by the collagen alone. Strain analysis was conducted in FIJI by measuring the relative displacement of glass beads. Sample strain was computed as a ratio of the change in distance between bead pairs to their initial separation. Load per unit area was calculated, and resulting stress-strain plots were generated in MATLAB (MathWorks, Natick, MA).

Multiphoton SHG imaging and CurveAlign analysis

Collagen gels were imaged via second harmonic generation (SHG), a technique that employs multiphoton microscopy to allow visualization of non-centrosymmetric molecules independent of fluorescence. Acquisition was conducted on WiscScan software and a Nikon 40x Apo water immersion lens (Numerical Aperture, N.A. 1.15 and Working Distance, W.D. 0.61) was used to visualize the organization of individual fibers in the matrix. Z-stacks consisting of an inter-plane spacing of no more than 10μm were collected to obtain an accurate depiction of fiber organization across gel thickness for collagen gels submitted for tensile testing and for collagen in microchannels. Images of collagen fibers were analyzed using CurveAlign software (www.loci.wisc.edu/software/curvelet-based-alignment-analysis) to measure the 2D-projected angles of all fibers relative to the horizontal, and to obtain a coefficient of alignment.

Microchannel migration assay

Microchannels with widths of 1mm and 3mm were fabricated using soft lithography according the protocol described in Sung, et al. (7). Briefly, SU8-100 was spun onto a silicon wafer to obtain a mold with channel thickness of 200μm. After UV exposure of the first layer, a second SU8-100 layer was spun to obtain a 200μm port layer. Polydimethylsiloxane (PDMS, Sylgard

184 Silicon Elastomer Kit, Dow Corning, Midland, MI) was molded over the master, and cured PDMS channels were adhered to glass bottom culture dishes (MatTek, Ashland, MA).

PDMS microchannels with the center cell port initially covered with a thin PDMS rectangle were first coated with 50μg/ml collagen in water for 1-2 hours, and then washed three times with PBS. Neutralized collagen solution containing penicillin/streptomycin was prepared and a droplet of 100-200μL was added to the flow inlet ports of the channels. The channels were then immediately placed at 4°C for overnight incubation to slow the polymerization kinetics and allow nucleation of short fibers (7). Immediately following incubation, a vacuum was applied to the outlet ports of wide channels to allow flow of collagen through the channels. After 2-3 minutes at room temperature, vacuum was applied to narrow channels to induce flow of collagen. An additional 2-3 minutes after collagen flow, thin PDMS rectangles were used to carefully cover both the inlet and outlet channel ports, after which the center cell port was uncovered. Covering the inlet and outlet ports prior to uncovering the center port allowed for minimal additional flow of collagen when center port was uncovered and cells added. A 1.5μL cell suspension of 5 x 10^6 cells/ mL was added to the center port. Channels were left undisturbed at room temperature for an additional 5 minutes, then placed in 37°C incubator for 10 minutes. All PDMS rectangular covers were removed and 2.5mL DMEM was added to the dish. For endpoint analysis, cells were allowed to migrate into channels for three days, then fixed with 4% paraformaldehyde for 10 minutes and then nuclei were stained with bis-benzimide. For time-lapse experiments, cells were imaged 2-3 days after they began migrating into the channels from the port. DMEM was replenished the night before imaging. For inhibitor experiments, either H1152 or ML-7 was added at a final concentration of 10μM or 2μM, respectively 30 minutes prior to imaging.

Confocal imaging

Channels for end point and time-lapse experiments were imaged using a Prairie Technologies point scanning inverted confocal microscope with PrairieView acquisition software (Prairie Technologies, Middleton, WI). A Nikon 10x Plan Fluor objective (N.A. 0.3 and W.D. 16) and 405nm laser line were used to image bis-benzimide stained nuclei, and serial images of cells that migrated out of the port were collected that were later compiled into montages of 3-9 images using a stitching algorithm in FIJI (8). For time-lapse experiments, DIC imaging combined with the 488nm laser line were used to image MDA-MB-231 cells and FITC-collagen, respectively. To observe cell migration, a Nikon 20x Plan Apo VC objective (N.A. 0.75 and W.D. 1) was used to collect images every 10 minutes for a period of 6 hours. To observe fiber displacement, a 20x objective with an optical zoom of 3 was used to collect images every 4 minutes for 2 hours. To observe cellular protrusions containing Lifeact-mRFP, a 20x objective with optical zoom of 3 and 561nm laser line was used to collect images every 4 minutes for 40 minutes. For all live imaging, a LiveCell (Pathology Devices, Westminster, MD) environmental chamber was used to maintain a constant 37°C, 5% CO_2, and 75% humidity for the duration of the experiment.

Cell migration analysis

For channel endpoint analysis, images were compiled into montages of 3-9 images using a stitching algorithm in FIJI. Nuclear stained images were segmented using the Yen algorithm and converted into a binary image for a nuclear object count. Bright field images of each channel were used to generate masks of 100μm-wide concentric rings surrounding the port, which were

intersected by the channel walls. Masks were applied to the montages containing the stained nuclei, and nuclei were counted using the 3D object counter plugin in FIJI. Nuclear counts were compiled and normalized to the area of the ring in which they were counted.

For time-lapse migration analysis, cells were tracked using the MTrackJ plugin in FIJI, and all x-y positions at each time point were recorded. Only individual cells were included in the analysis to eliminate confounding data from cell-cell interactions or collective migration. In some cases, a small, but significant amount of image drift occurred in the x-y plane. To compensate for this, a fiduciary marker in the form of a particle > 100μm from the nearest cell, or region of the channel wall or port was tracked for all images collected. The image drift was then computed and subtracted from the positions of each cell in the image. Only cells that remained in the field of view for the entire experiment were analyzed, and non-motile or dividing cells were excluded. A non-motile cell was defined as one that did not translocate more than one cell length in distance, or about 20μm for the duration of the time-lapse. For experiments involving the ROCK inhibitor, H1152, very little to no migration was observed. In order to maintain consistency in the numbers of cells analyzed per image, the percentage of cells that corresponded to the motile fraction (about 65% of cells in each image) of untreated cells was used to analyze images of H1152 treated cells.

Cell position data was then used to calculate speed and persistence. Speed was computed as the total track length divided by time, and therefore represented an average speed over the entire track. Direction-dependent speed in narrow channels was not measured as the tracks were predominantly parallel to the direction of alignment. Chemotactic index, given by: $CI = \left(\frac{Net\ Displacement}{Total\ Track\ Length}\right)\cos\alpha$, was used as a measure of cellular persistence relative to the orientation of aligned collagen. Measurements were made over the same interval of time to normalize the time component of *CI*. In the expression of CI, α represents the angle between the net migration vector and the channel wall, which corresponds to the direction of alignment in narrow channels. In order to account for the observation that more cells in narrow channels often reversed direction multiple times along aligned collagen fibers, which would have a significant effect on the magnitude of their net migration vector, the absolute value of all net displacements for cells in both narrow and wide channels was used to compute *CI*.

Collagen fiber tracking analysis

Images of FITC-labeled collagen fibers were analyzed in FIJI using the MTrackJ plugin. Fiber junctions or regions of fibers that were clearly present in all images were used for tracking. Image drift was calculated in a similar fashion to the migration analysis by tracking either a stationary collagen fiber at least 50μm away from the nearest cell, or a stationary object in the corresponding bright field image. Fiber positions were calculated by subtracting the image drift, and a sum total of the fiber displacement for the duration of the 2-hour imaging experiment was computed.

2D migration experiments on polyacrylamide gels

Cell migration experiments on 2D polyacrylamide (PA) gels were carried out according to other reports (9-11). The amount of added bis-acrylamide cross-linker resulted in PA gels of different stiffness. The 10KPa and 44KPa gel stiffness conditions were chosen to correspond to the measured moduli of unfixed 1mg/ml and 4mg/ml collagen gels from Roeder et al. (5). A

100KPa condition was also added to correspond to the estimated modulus of an unfixed aligned 4mg/ml collagen gel. The ratio of acrylamide to bis-acrylamide for gels of different stiffness was calculated from (9). PA gels were further cross-linked with sulfo-SANPAH (Pierce) under UV for 90 seconds, and 500μL of a 200μg/mL collagen in water solution was added to the gels for 2 hours at room temperature. For experiments where collagen concentration was varied instead of gel stiffness, 10KPa gels were used and collagen concentrations of 50μg/mL and 400μg/mL were added to the gel. Gels were carefully rinsed with PBS three times and sterilized under UV for 30 minutes. 10,000 MDA-MB-231 cells were seeded onto the surface of PA gels and allowed to adhere overnight. Confocal time-lapse experiments of migrating cells were conducted the following day.

Cell migration model

A computational model of cell migration as a function of time was developed using MATLAB (MathWorks). To correspond to the 2D measurements of cell migration in 3D narrow and wide microchannels, cell displacements were computed in one plane from an initial random generation of protrusion vector magnitudes, P, and orientations, θ. Cells were defined to contain up to 30 arbitrary protrusion vectors to simulate the likely opposing forces produced from pseudopods and associated adhesions (12). Protrusion vectors were therefore limited to defined orientations or "slots" in 12° increments, or 360°/30, distributed around the cell. At each time step, the magnitudes and protrusion vector slot orientations were randomly determined. A vector sum was then computed, which resulted in the distance traveled by the cell at that time step. To simulate the observation that cellular adhesions are stabilized and likely maintained by mechanical force (13), we used a threshold for protrusion vector magnitudes to allow the orientations of some vectors to persist into the next time step. Vectors with magnitudes above the threshold (85% of vectors), maintained their orientations for the next time step, while vectors with magnitudes below the threshold (15% of vectors) had their orientations re-randomized for the next time step. This allowed representation of both stabilized and dynamic protrusions, resulting in the simulated cells making several persistent consecutive moves, and less dramatic changes in direction to better correspond with our observations in 3D collagen gels. All protrusion vector magnitudes were re-randomized at every time step.

With this simplified model of randomly generated protrusion vector magnitudes and orientations, we varied the number of protrusion vectors and computed the resulting cell speed over 36 time steps. The model produced a bimodal relationship between speed and the number of protrusion vectors (Figure S2 *A*). This initial result mimics the biphasic nature of migration speed with integrin expression (14), and serves to validate our approach of using randomized protrusion vectors to simulate cell movement.

In order to make comparisons of cell migration in 3D matrices with varying physical and mechanical properties, we incorporated model coefficients to represent matrix stiffness, ligand density, and alignment that were defined to be dependent on the measured experimental conditions. These coefficients were then used to modify the components of the protrusion vectors prior to the computed vector sum at each time step. Equations for the parallel and perpendicular components of the matrix-modified protrusion vectors ($P_{M_\parallel}$ and $P_{M_\perp}$) with respect to the direction of alignment are given by:

$$P_{M_\parallel} = P_\parallel \left(\frac{C_S}{C_{LD}(1-C_A)}\right) \text{ and } \quad P_{M_\perp} = P_\perp \left(\frac{C_S(1-C_A)}{C_{LD}}\right)$$

where C_S is the coefficient of matrix stiffness, C_A is the model coefficient of alignment, and C_{LD}, is the coefficient of ligand density. As C_A approached zero, representing a random matrix, equations for $P_{M_\parallel}$ and $P_{M_\perp}$ reduced to an identical expression, one that was only dependent on matrix stiffness and ligand density.

Relationships for the model coefficients and the measured experimental conditions are shown in Fig. S2 *B-D*, and were determined using an iterative approach that consisted of varying each parameter independently to determine the effects on the others. Additionally, the number of protrusion vectors was assumed to depend on alignment and ligand density (Fig. S2 *E*) and was computed for each set of matrix conditions.

To better model the increased cellular persistence seen with increasing matrix alignment, we incorporated a probability that cells will continue in their initial randomly determined direction as a function of increasing alignment. We computed the protrusion vector orientation slot that was nearest the cell's net displacement vector at each time step. All floating vectors had a greater probability of either falling within this slot, or the nearest 3 slots on either side of it unless they were already occupied. If all of these "persistent" slots were filled, remaining vectors were randomly assigned to any open slot around the cell. The probability of filling persistent slots increased as a linear function of C_A, and increased cellular persistence was simulated in this way at every time step.

All model parameters used are tabulated in Table S1.

Protrusion analysis

Time-lapse confocal images (Fig. *S3A*) were thresholded in FIJI using the Huang algorithm (Fig. *S3B*) and analyzed for number and length of protrusions at each time point using custom MATLAB code. For each cell, the locations of the centroids and boundary pixels were identified. From the boundary pixels, the perimeter was determined, and the number of equally spaced perimeter nodes was defined as a linear function of perimeter. This ensured that cells having different perimeters would have similar perimeter node spacing. Once the perimeter nodes were determined, sharp convex regions in boundary curvature were identified by summing the exterior angles of the 5 subsequent nodes at each node of the enclosed polygon. Any sum of five nodes that resulted in an angle greater than 105° was considered a convex region. Where there were consecutive nodes with sums greater than this threshold, the algorithm searched for the position of the starting node that resulted in the greatest sum. The tip of the protrusion was then determined by finding the maximum external angle formed between any three nodes within the identified convex region. Finally, in order to better distinguish between protrusions and regions of the cell that were only moderately convex, the smallest circle containing the tip of the protrusion and the adjacent two nodes on either side was computed. If the radius of the circle was greater than 2μm, the convex region was not counted as a protrusion. All boundary nodes and identified protrusions were overlaid onto all thresholded images of cells (Fig. *S3C*) and lengths of protrusions relative to the cell centroid were computed. In order to determine the accuracy of the algorithm at identifying protrusions, 5 panelists were given 26 thresholded images of cells and asked to identify all protrusions. Tested against the results from the panelists, the algorithm identified protrusions for each cell that fell within the range of responses

on average 93% of the time. All cells imaged in both narrow and wide channels were then analyzed using this approach.

Statistics

All statistics were computed using a two-sided Wilcoxon Rank Sum test using Mstat software (McArdle Laboratory for Cancer Research, Madison, WI). Differences in the data were deemed significant if a P-value < 0.05 was obtained. All significant differences were denoted with an asterisk (*) in the corresponding figures.

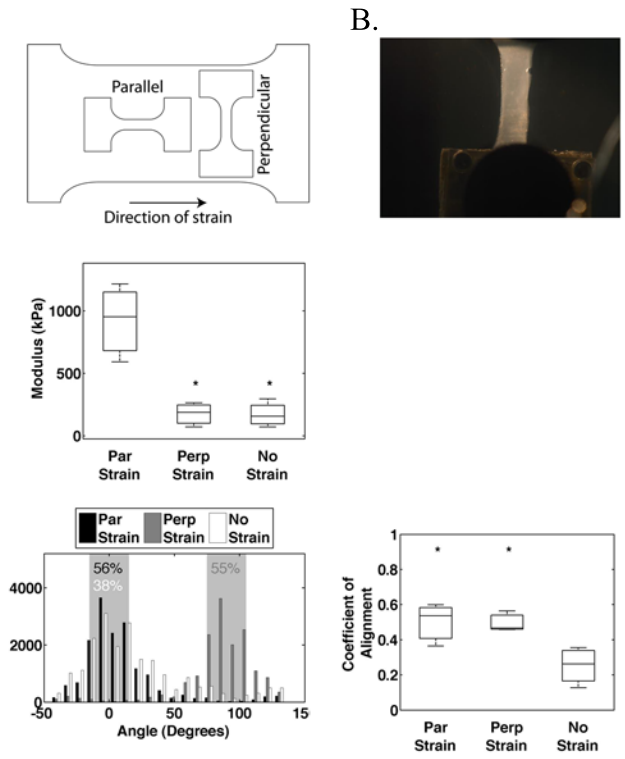

Figure S1. Aligned collagen is stiffest along the axis of alignment. *(A)* Diagram of test conditions. Large collagen dogbone gels are cast and subjected to 30% strain. After fixing with 4% PFA, two dogbone test specimens are cut parallel and perpendicular to the strained axis. *(B)* Image of gauge region of dogbone-shaped collagen gel in one grip of the Instron. Extreme care was taken to load gels into grips without damaging gels. *(C)* Tensile modulus of unstrained, parallel strained and perpendicular strained gels fixed with PFA, n=3 gels, $p < 0.05$. *(D, left)* Histograms of fiber angles generated from CurveAlign software of unstrained, parallel strained *(Par Strain)*, and perpendicular strained *(Perp Strain)* gels. Percentages represent the fraction of fiber angles ±15° from 0° and 90° *(shaded regions)*. *(D, right)* Coefficient of alignment of unstrained, parallel strained, and perpendicular strained gels, n=3, $p < 0.05$.

Fig. S2

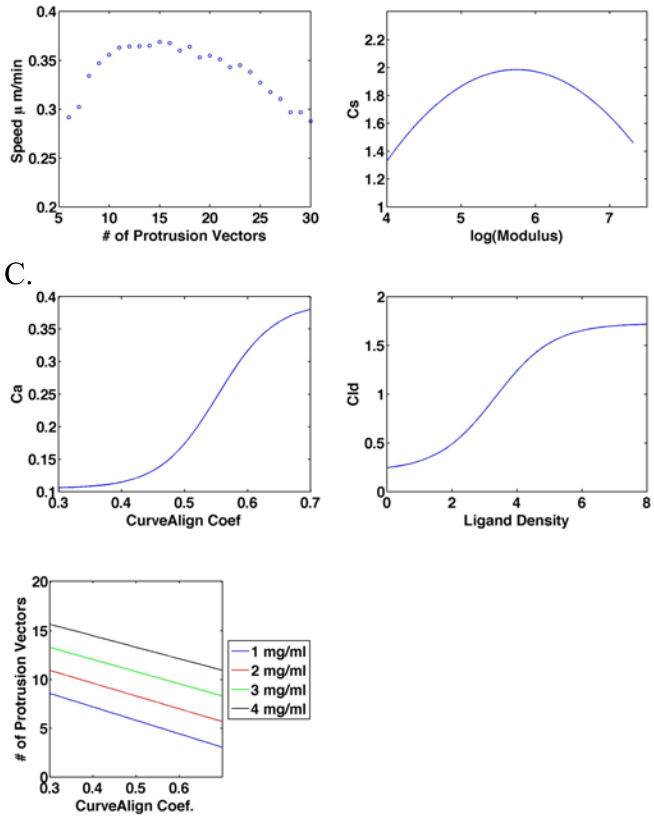

Figure S2. Migration model coefficient relationships. *(A)* Model predicts migration speed is biphasic with the number of cell protrusion vectors. *(B)* Model relationships between experimental conditions and model coefficients for Coefficient of Stiffness, *(C)* Coefficient of Alignment, and *(D)* Coefficient of Ligand Density. *(E)* Model relationship showing a linear dependence of the number of protrusion vectors on alignment for various collagen densities.

Table S1

Model Parameters	Variable Name	Value(s)
Protrusion vector	P	0 – 0.7
Vector orientation slot	θ	(12 – 30) × 12°
Vector threshold	Th	0.15 × PV
Stiffness	S	70 – 1000
Coefficient of stiffness	C_S	1.5 – 2
CurveAlign coefficient	A	0.3 – 0.7
Coefficient of alignment	C_A	0.1 – 0.4
Ligand density	LD	1 – 4
Coef. of ligand density	C_{LD}	0.25 – 1.25
# of protrusion vectors	N_P	3 – 27

Table S1. Migration model input parameters. Values and ranges are listed for all input parameters used in the model.

C.

Figure S3. Cell protrusion analysis. *(A)* Confocal images of MDA-MB-231 cells expressing Lifeact-mRFP in narrow *(left panel)* and wide *(right panel)* channels. *(B)* Thresholded images and *(C)* output images from custom MATLAB code showing the equally spaced nodes on the cell boundary *(blue circles)* and the number and location of identified protrusions *(red circles)*.

Movie S1. 6-hour confocal time-lapse images of MDA-MB-231 cells migrating in wide (*top panels*) and narrow (*bottom panels*) microchannels. DIC images (*left panels)* and fluorescence

images of FITC-labeled collagen fibers (*right panels*) were collected at 10-minute intervals, scale bar, 500μm.

Movie S2. 2-hour confocal time-lapse images of MDA-MB-231 cells displacing collagen fibers in wide (*top panels*) and narrow (*bottom panels*) microchannels. DIC images (*left panels)* and fluorescence images of FITC-labeled collagen fibers (*right panels*) were collected at 4-minute intervals, scale bar, 200μm.

Movie S3. 40-minute confocal time-lapse images of MDA-MB-231 cells expressing Lifeact-mRFP to visualize protrusions in narrow *(top)* and wide *(bottom)* microchannels. Scale bar, 20μm.

Matlab code for model of cell migration in aligned collagen

```
% Cell Migration Parameter Model

% 3D cell migration is modeled by measureable inputs: Vc = discrete cell
% displacement, A = collagen alignment, Ld = ligand density, S = collagen
% matrix stiffness; unknown inputs dependent on measureable inputs: Cs =
% stiffness coefficient, Cc = confinement coefficient (inverse of porosity), GH = number of
% protrusion vectors per cell, Ca = alignment coefficient; and random inputs:
% Theta = random initial direction of grappling hook, Vh = random magnitude
% of pull per protrusion vector

%%% Model Inputs

t=36; % Number of time points
n=100;  % Number of iterations
int = 10;   % Time interval (in minutes)
Vcmax = .7;
Vcmin = 0.15*Vcmax;

%%% Empirically determined model relationships

Sa = 1000;   % alignment modulus in KPa
Sr = 225;   % random modulus in KPa ~ perpendicular modulus

y03 = -5.1136;
a3 = 2.469;
b3 = -.2147;

Csa = y03 + a3*log(Sa) + b3*log(Sa)^2;
Csr = y03 + a3*log(Sr) + b3*log(Sr)^2;

Aa = 0.7; % From CurveAlign analysis
Ar = 0.3;
Ar0 = 0;
```

```
a = .2868;
b = .0457;
x0 = .5526;
y0 = .1047;
Ca = y0 + a/(1+exp(-(Aa-x0)/b));
Cr = y0 + a/(1+exp(-(Ar-x0)/b));
Cr0 = y0 + a/(1+exp(-(Ar0-x0)/b));

Ld =4;  % in mg/ml
y01 = .2096;
x01 = 3.3376;
a1 = 1.5142;
b1 = .8909;
Ccld  = y01 + a1/(1+exp(-(Ld-x01)/b1));

GHa = round((.6667*Ld-14.4667)*Aa+(2.1667*Ld+10.5333))
GHr = round((.6667*Ld-14.4667)*Ar+(2.1667*Ld+10.5333))

proba = [.5+(Ca-Cr0) .5-(Ca-Cr0)]
probr = [.5+(Cr-Cr0) .5-(Cr-Cr0)]

%%% Aligned Case

Dx=zeros(t,n);
Dy=zeros(t,n);
X=zeros(t,n);
Y=zeros(t,n);
R=zeros(t,n);
alpha=zeros(t,n);

for k=1:n

   nearRslots = 0;
   Thetapos = randperm(30)';
   Theta = Thetapos(1:GHa).*12;

   for i=1:t

      Vh = rand(GHa,1)*Vcmax;
      Vhx = Vh.*cos(Theta.*pi/180);
      Vhy = Vh.*sin(Theta.*pi/180);
      Fx = Vhx.*Csa*1/(Ccld*(1-Ca));
      Fy = Vhy.*Csr*(1-Ca)/Ccld;
      Rx=0;
      Ry=0;
      Thetanew=zeros(GHa,1);
```

```
for j=1:GHa

   Rx=Rx+Fx(j);
   Ry=Ry+Fy(j);

   if Vh(j) >= Vcmin

      Thetanew(j)=Theta(j);
   end
end

Dx(i,k)=Rx;
Dy(i,k)=Ry;
R(i,k)=sqrt(Rx^2+Ry^2);
alpha(i,k)=atan(Ry/Rx)*180/pi;

if Rx < 0 && Ry > 0
   alpha(i,k) = alpha(i,k) + 180;
elseif Rx < 0 && Ry < 0
   alpha(i,k) = alpha(i,k) + 180;
elseif Rx > 0 && Ry < 0
   alpha(i,k) = alpha(i,k) + 360;
end

Alpha = alpha(i,k);
slotdir = 12:12:360;
Rslot = find((slotdir < Alpha & slotdir > Alpha-6) | (slotdir > Alpha & slotdir < Alpha+6));
newGH = length(find(Thetanew==0));
nearRslots = Rslot*12-3*12:12:Rslot*12+3*12;

openslots = find(ismember(nearRslots,Thetanew)==0);
openslotdir = nearRslots(openslots);

if length(newGH)>length(openslotdir) && newGH ~=0
   Thetanew = [Thetanew; openslotdir'];
elseif length(newGH)<length(openslotdir) && newGH ~=0
   slotprob=[ones(length(openslotdir),1).*proba(1)/length(openslotdir);proba(2)];
   for q=1:length(newGH)
      r=rand;
      x = sum(r >= cumsum([0; slotprob]));
      for z=1:length(openslotdir)
         if z==x
            Thetanew=[Thetanew; openslotdir(z)];
         end
      end
```

```
        end
    end

    Thetanew(Thetanew==0)=[];
    thetanew=Thetanew./12;
    newThetapos = randperm(30)';
    norepeats=find(ismember(newThetapos,thetanew)==0);
    newThetapos=newThetapos(norepeats);
    if GHa-length(Thetanew) == 0
        Theta = Thetanew;
    else
        T = newThetapos(1:GHa-length(Thetanew)).*12;
        Theta=[Thetanew; T];
    end

  end

  for i=2:t+1

    X(i,k) = Dx(i-1,k)+X(i-1,k);
    Y(i,k) = Dy(i-1,k)+Y(i-1,k);

  end

end

NetDispA = sqrt((X(size(X,1),:)-X(1,:)).^2+(Y(size(Y,1),:)-Y(1,:)).^2);
SpeedA = sum(R,1)/(t*int);

AbsNetAlphaa = atan(sum(abs(Dy))./sum(abs(Dx)));

CIa = sqrt((sum(abs(Dx))).^2+(sum(abs(Dy))).^2)./sum(R).*cos(AbsNetAlphaa);

%%% Random Case

Dx=zeros(t,n);
Dy=zeros(t,n);
X=zeros(t,n);
Y=zeros(t,n);
R=zeros(t,n);
alpha=zeros(t,n);

for k=1:n

  nearRslots = 0;
  Thetapos = randperm(30)';
```

```
Theta = Thetapos(1:GHr).*12;

for i=1:t

    Vh = Vcmax*rand(GHr,1);
    Vhx = Vh.*cos(Theta.*pi/180);
    Vhy = Vh.*sin(Theta.*pi/180);
    Fx = Vhx.*Csr*1/(Ccld*(1-Cr));
    Fy = Vhy.*Csr*(1-Cr)/Ccld;
    Rx=0;
    Ry=0;
    Thetanew=zeros(GHr,1);

    for j=1:GHr

        Rx=Rx+Fx(j);
        Ry=Ry+Fy(j);

        if Vh(j) >= Vcmin

            Thetanew(j)=Theta(j);
        end
    end

    Dx(i,k)=Rx;
    Dy(i,k)=Ry;
    R(i,k)=sqrt(Rx^2+Ry^2);
    alpha(i,k)=atan(Ry/Rx)*180/pi;

    if Rx < 0 && Ry > 0
        alpha(i,k) = alpha(i,k) + 180;
    elseif Rx < 0 && Ry < 0
        alpha(i,k) = alpha(i,k) + 180;
    elseif Rx > 0 && Ry < 0
        alpha(i,k) = alpha(i,k) + 360;
    end

    Alpha = alpha(i,k);
    slotdir = 12:12:360;
    Rslot = find((slotdir < Alpha & slotdir > Alpha-6) | (slotdir > Alpha & slotdir < Alpha+6));
    newGH = length(find(Thetanew==0));
    nearRslots = Rslot*12-3*12:12:Rslot*12+3*12;

    openslots = find(ismember(nearRslots,Thetanew)==0);
    openslotdir = nearRslots(openslots);
```

```
        if length(newGH)>length(openslotdir) && newGH ~=0
            Thetanew = [Thetanew; openslotdir'];
        elseif length(newGH)<length(openslotdir) && newGH ~=0
            slotprob=[ones(length(openslotdir),1).*probr(1)/length(openslotdir);probr(2)];
            for q=1:length(newGH)
                r=rand;
                x = sum(r >= cumsum([0; slotprob]));
                for z=1:length(openslotdir)
                    if z==x
                        Thetanew=[Thetanew; openslotdir(z)];
                    end
                end
            end
        end

        Thetanew(Thetanew==0)=[];
        thetanew=Thetanew./12;
        newThetapos = randperm(30)';
        norepeats=find(ismember(newThetapos,thetanew)==0);
        newThetapos=newThetapos(norepeats);
        if GHr-length(Thetanew) == 0
            Theta = Thetanew;
        else
            T = newThetapos(1:GHr-length(Thetanew)).*12;
            Theta=[Thetanew; T];
        end

    end

    for i=2:t+1

        X(i,k) = Dx(i-1,k)+X(i-1,k);
        Y(i,k) = Dy(i-1,k)+Y(i-1,k);

    end

end

NetDispR = sqrt((X(size(X,1),:)-X(1,:)).^2+(Y(size(Y,1),:)-Y(1,:)).^2);
SpeedR = sum(R,1)/(t*int);

AbsNetAlphar = atan(sum(abs(Dy))./sum(abs(Dx)));

CIr = sqrt((sum(abs(Dx))).^2+(sum(abs(Dy))).^2)./sum(R).*cos(AbsNetAlphar);

Speed = [SpeedA' SpeedR'];
```

CI = [CIa' CIr'];

Supporting References

1. Heck, J. N., S. M. Ponik, M. G. Garcia-Mendoza, C. A. Pehlke, D. R. Inman, K. W. Eliceiri, P. J. Keely. 2012. Microtubules regulate GEF-H1 in response to extracellular matrix stiffness. Mol Biol Cell. 23:2583-2592.
2. Vader, D., A. Kabla, D. Weitz, L. Mahadevan. 2009. Strain-induced alignment in collagen gels. PLoS One. 4:e5902.
3. Chua Chee, K. 1994. Three-dimensional rapid prototyping technologies and key development areas. Computing & Control Engineering Journal. 5:200-206.
4. Wozniak, M. A., P. J. Keely. 2005. Use of three-dimensional collagen gels to study mechanotransduction in T47D breast epithelial cells. Biol Proced Online. 7:144-161.
5. Roeder, B. A., K. Kokini, J. E. Sturgis, J. P. Robinson, S. L. Voytik-Harbin. 2002. Tensile mechanical properties of three-dimensional type I collagen extracellular matrices with varied microstructure. J Biomech Eng. 124:214-222.
6. Lopez-Garcia, M. D., D. J. Beebe, W. C. Crone. 2010. Young's modulus of collagen at slow displacement rates. Biomed Mater Eng. 20:361-369.
7. Sung, K. E., G. Su, C. Pehlke, S. M. Trier, K. W. Eliceiri, P. J. Keely, A. Friedl, D. J. Beebe. 2009. Control of 3-dimensional collagen matrix polymerization for reproducible human mammary fibroblast cell culture in microfluidic devices. Biomaterials. 30:4833-4841.
8. Schindelin, J., I. Arganda-Carreras, E. Frise, V. Kaynig, M. Longair, T. Pietzsch, S. Preibisch, C. Rueden, S. Saalfeld, B. Schmid, J. Y. Tinevez, D. J. White, V. Hartenstein, K. Eliceiri, P. Tomancak, A. Cardona. 2012. Fiji: an open-source platform for biological-image analysis. Nat Methods. 9:676-682.
9. Yeung, T., P. C. Georges, L. A. Flanagan, B. Marg, M. Ortiz, M. Funaki, N. Zahir, W. Ming, V. Weaver, P. A. Janmey. 2005. Effects of substrate stiffness on cell morphology, cytoskeletal structure, and adhesion. Cell Motil Cytoskeleton. 60:24-34.
10. Pelham, R. J., Jr., Y. Wang. 1997. Cell locomotion and focal adhesions are regulated by substrate flexibility. Proc Natl Acad Sci U S A. 94:13661-13665.
11. Aratyn-Schaus, Y., P. W. Oakes, J. Stricker, S. P. Winter, M. L. Gardel. 2010. Preparation of complaint matrices for quantifying cellular contraction. J Vis Exp.
12. Schoen, I., B. L. Pruitt, V. Vogel. 2013. The Yin-Yang of Rigidity Sensing: How Forces and Mechanical Properties Regulate the Cellular Response to Materials. Annual Review of Materials Research. 43:589-618.
13. Smith, A. S., K. Sengupta, S. Goennenwein, U. Seifert, E. Sackmann. 2008. Force-induced growth of adhesion domains is controlled by receptor mobility. Proc Natl Acad Sci U S A. 105:6906-6911.
14. Huttenlocher, A., A. R. Horwitz. 2011. Integrins in cell migration. Cold Spring Harb Perspect Biol. 3:a005074.